HUGHES

HUGHES AIRCRAFT COMPANY
RESEARCH LABORATORIES

INTEGRATED OPTIC WAVEGUIDE DEVICES

FINAL REPORT

O. Glenn Ramer

May 1980

JPL Contract Number 955291

Hughes Research Laboratories
3011 Malibu Canyon Road
Malibu, California 90265

This work was performed for the Jet Propulsion Laboratory, California Institute of Technology sponsored by the National Aeronautics and Space Administration under Contract NAS7-100.

TABLE OF CONTENTS

LIST OF ILLUSTRATIONS

SECTION 1

INTRODUCTION AND SUMMARY

The objectives of this program were to design, fabricate, test, and deliver integrated optic (IO) waveguide circuits with a phase bias element and modulator switch on the same chip. The chips were to be addressed by single-mode fibers, with fiber pigtails affixed to the chips. The intended application for these chips is the fiber-optic rotation sensor (FORS). It is felt that IO is indispensable to the achievement of a high-performance FORS: alignment difficulties and severe vibration problems preclude development of a conventional bulk optical system. A block diagram of the FORS system under development by JPL[1] is shown in Figure 1.

The four IO waveguide chips each consist of an electrically actuated planar waveguide 2 x 2 switch, a planar waveguide phase shifter incorporated into one waveguide leg, and attached pigtails. A photograph of a device is shown in Figure 2. The performance goals were: switching isolation of 17 dB or greater, with a switch voltage less than 50 V for 0.85-μm operation; a phase shift of $\pi/2$ in response to 15 V or less for 0.85-μm operation; polarization preservation with a polarization ratio of at least 10; and transmission from fiber input to fiber output for either channel and for either switch state of 20% or greater for 0.85-μm operation. Strain reliefs for the electrical loads were to be incorporated so that a transient pull of 100 g would not cause separation and so that, for the fiber pigtail, a transient pull of 100 g would not cause damage and a transient pull of 20 g would not affect the coupling.

The technology development was divided into two phases: chip development (involving the development of the IO chip with the 2 x 2 switch and phase shifter combination) and fiber-to-chip interfacing (involving the permanent coupling of single-mode fiber-optic pigtails to the four ports of the chip). The theory and design involved in these phases are described in detail in Section 2. Briefly, the switch format was based on coherent coupling between waveguides formed in Z-cut $LiNbO_3$. The control of the coupling was achieved by electrooptically varying the

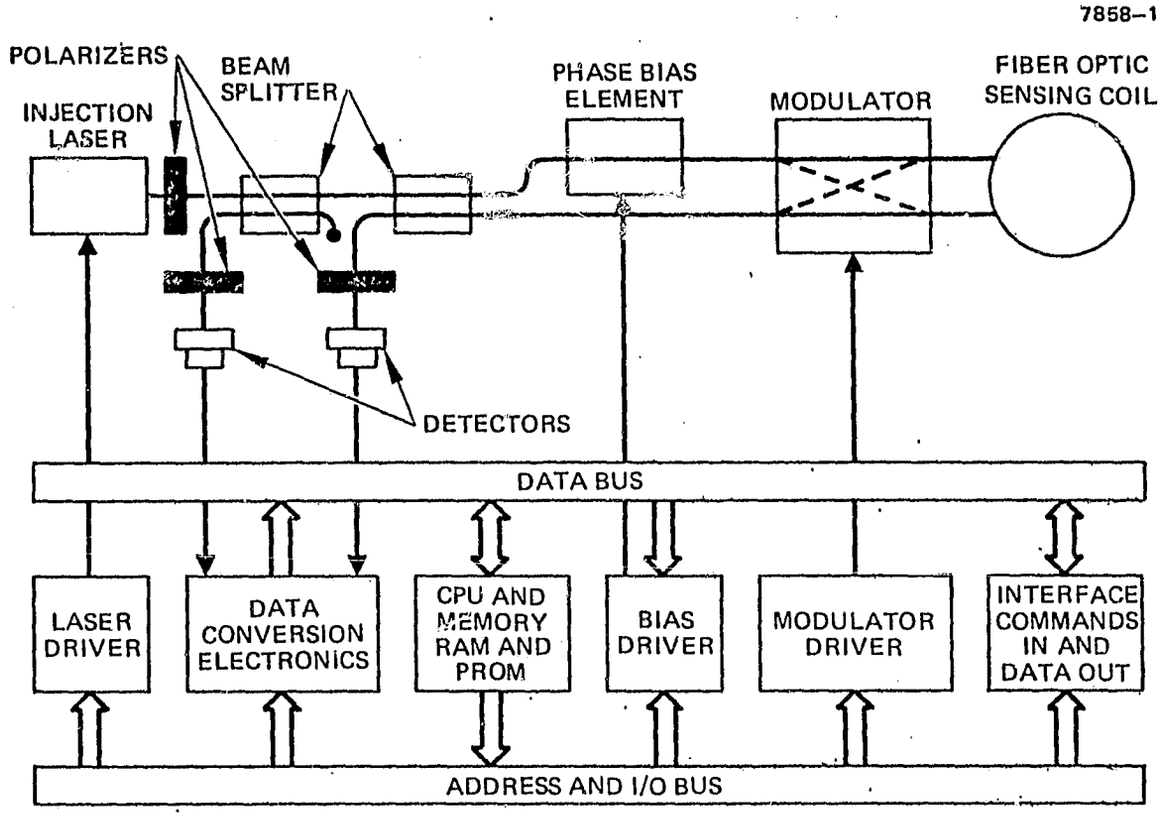

Figure 1. Typical FORS block diagram.

M13359

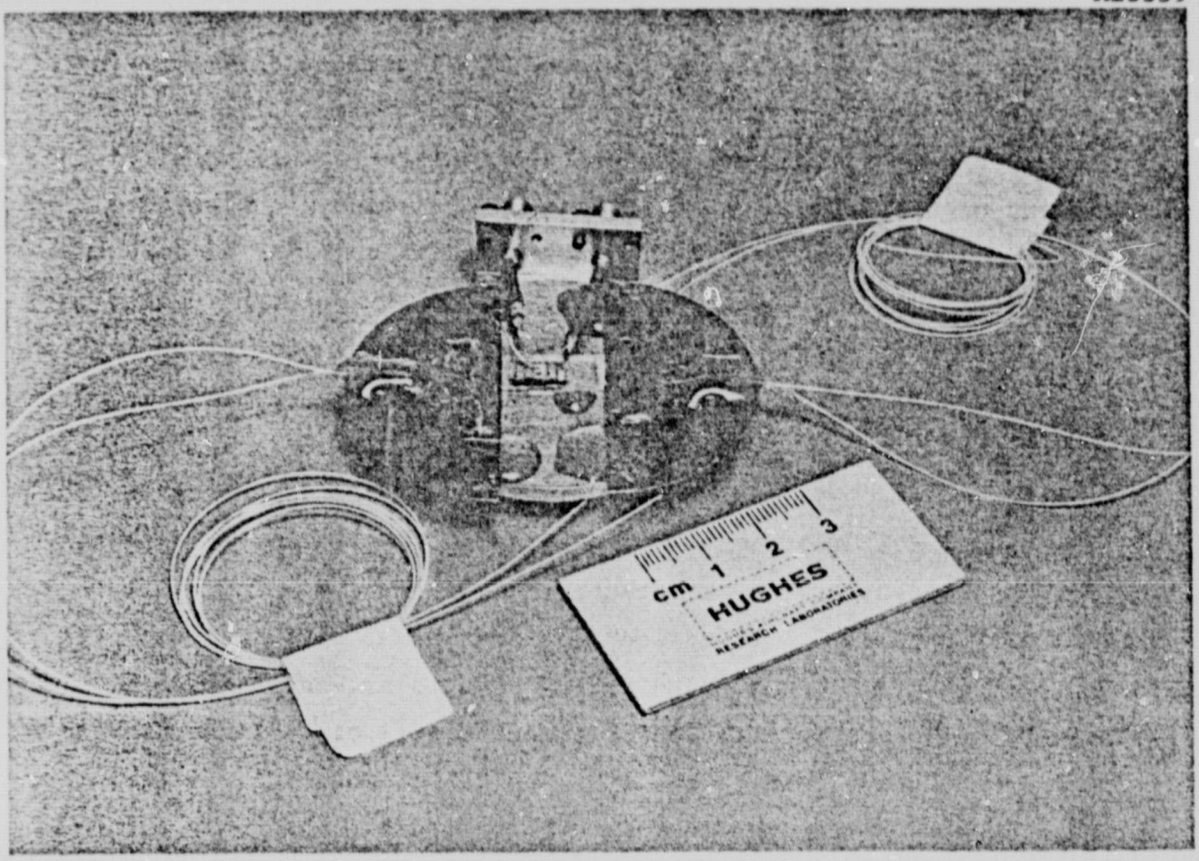

Figure 2. Photograph of fiber-optic switch with attached pigtails.

phase propagation constants of each guide. The electrode arrangement divides the coupler into two equal-length sections (Figure 3), such that the $\Delta\beta$ reversal[2] technique could be used to achieve both the bar state (straight through propagation) or the cross state. Using this technique, all the switch goals of the program were achieved. The goals for the phase shifter were achieved by electrooptically varying the phase propagation constant of one guide independent of the other.

The second technical area, fiber-to-chip interfacing, required the development of appropriate fixturing and manipulation techniques to achieve the close tolerance requirements for high coupling efficiency between a fiber with an $\sim$5-μm core and a channel guide with roughly a 2-μm by 5-μm cross section. Although the theoretical prediction for butt coupling efficiency was $\sim$0.7 (1.5 dB loss), the best results achieved to date for staight channel guides has been a 3.7 dB coupling loss. This measurement was made with a single-mode fiber butted to the edge of the channel guide and a microscope objective to collect the output light. The following losses were subtracted from the collected throughput: 1 dB microscope loss, 0.5 dB reflection loss from the $LiNbO_3$ edge, and 1 dB guide propagation loss.* The source of this excess loss is believed to be in the preparation of interfaces (i.e., polished surfaces of the fiber and chip) and in the fiber holder or mounting fixture. Further development is required in this area before all the goals of the program can be achieved (see Section 4). The best throughput loss measured to date for a fiber pigtailed switch has been 11 dB, or 7.0% throughput; a more typical value was 14 dB. Although this major loss is at the fiber-to-chip interfaces, other sources of loss are propagation loss ($\sim$1 dB), electrode loss (3.6 dB), and reflection losses (0.5 dB). The mechanical fixturing for the coupling between the fiber and the $LiNbO_3$ chip met all the goals of the program.

*Note added in proof: Butt coupling losses to straight channel waveguides as low as 1 dB have been observed since the initial writing of this report. This value is approaching the theoretical optimum.

Section 2 presents the component design and operation principles for the switch, phase shifter, and fiber-to-chip coupling. Section 3 summarizes the performance of the delivered items. Section 4 outlines the technology development required for significant performance improvement of the IO chips.

6574-3

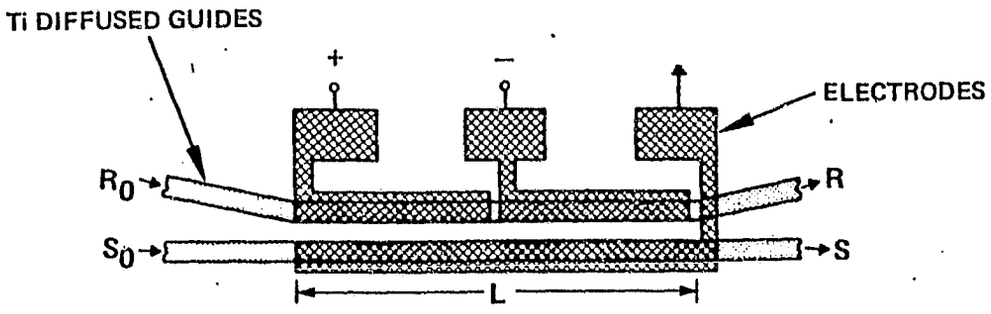

Figure 3. Schematic of a directional coupler with $\Delta\beta$ reversal.

SECTION 2

COMPONENT DESIGN AND OPERATION PRINCIPLES

A. SWITCH DESIGN

1. Switch Operation

The operation of the directional coupler switch is based on the coherent exchange of radiation between two single-mode channel waveguides of width W placed in close proximity (i.e., separated by a gap G) and configured so as to run parallel over an interaction length L (Figure 3). The waveguide patterns are formed in $LiNbO_3$ by diffusion of Ti with thickness d. An electrode arrangement divides the coupler into two equal-length sections in which voltages of equal or opposite sign can be applied to electrooptically (Pockels effect) control the phase propagation constants of each guide. With equal magnitude and opposite voltages applied to each section, a propagation constant mismatch $(\beta_1 - \beta_2) = \Delta\beta$ is imposed in the first half of the switch, and $-\Delta\beta$ is imposed in the second half. By adjusting the voltage, complete crossover and straight-through propagation can be obtained.

The manner in which a light beam couples its energy back and forth between two parallel dielectric channels can be completely characterized by three parameters: L, $\Delta\beta$, and κ. The parameter κ is a measure of the strength of the interchannel coupling. The physical interpretation of κ is simplified by considering the situation $\Delta\beta = 0$; in this case, the distance ℓ over which 100% power transfer occurs is given by $\ell = \pi/2\kappa$. In the single-electrode designs of a directional coupler, the transfer is controlled by spoiling the conditions of $\Delta\beta = 0$ or $\ell = \pi/2\kappa$. For optimum operation, the device must have a length equal to $n\ell$, where n is an odd integer. The exact attainment of both $\Delta\beta = 0$ and $L = \pi/2\kappa$ makes fabrication of a 100% transfer device very difficult. These requirements are relaxed by using the $\Delta\beta$-reversal configuration developed by Schmidt and Kogelnik.[2]

The switching action can be modeled by solving the coupled-mode equations

$$R' - j\delta R = j\kappa S \tag{1}$$

$$S' + j\delta R = j\kappa R \ , \tag{2}$$

where $\delta \equiv (\beta_1 - \beta_2)/2$, and the primed quantities refer to the spatial derivative d/dz (z being the direction of propagation). For the two-section switch shown in Figure 3, the solutions written in matrix form are, for arbitrary input amplitudes R_o and S_o and device length $2Z = L$,

$$\begin{bmatrix} R \\ S \end{bmatrix} = \begin{bmatrix} A_2 & -jB_2 \\ -jB_2^* & A_2^* \end{bmatrix} \begin{bmatrix} R_o \\ S_o \end{bmatrix} = \underbrace{\begin{bmatrix} A_1^* & -jB_1 \\ -jB_1^* & A_1 \end{bmatrix}}_{-\delta \text{ SECTION}} \underbrace{\begin{bmatrix} A_1 & -jB_1 \\ -jB_1^* & A_1^* \end{bmatrix}}_{+\delta \text{ SECTION}} \begin{bmatrix} R_o \\ S_o \end{bmatrix} \tag{3}$$

where

$$A_2 = 1 - 2\,B_1^{\,2} \tag{4}$$

$$B_2 = 2A_1^*\,B_1 \tag{5}$$

$$A_1 = \cos z\,(\kappa^2 + \delta^2)^{1/2} + j\delta \sin\left(z(\kappa^2+\delta^2)^{1/2}\right)/(\kappa^2 + \delta^2)^{1/2} \tag{6}$$

$$B_1 = \kappa \sin\left(z(\kappa^2 + \delta^2)^{1/2}\right)/(\kappa^2 + \delta^2)^{1/2} \tag{7}$$

$$\delta = \Delta\beta/2 \ . \tag{8}$$

The coefficients A_1 and B_1 are the elements in a matrix similar to Eq. 2 for the single electrode switch.

Assuming initial conditions with $(R_o, S_o) = (1, 0)$, corresponding to all power being initially in one guide, zero crosstalk in the crossed or parallel states is assured by setting $A_2 \equiv 0$ and $B_2 \equiv 0$, respectively. Each of these conditions establishes a correspondence between the normalized parameters L/ℓ and $\Delta\beta/L$; this correspondence is plotted in Figure 4. The interpretation of this switch diagram is straightforward. If L/ℓ is between 1 and 3, there exist values of $\Delta\beta$ (a function of the applied voltage or electric field under the electrodes) that will drive the device onto both the parallel and crossed curves. Thus, device length is a noncritical parameter, just as it is in a single-electrode switch. Switch diagrams for 1, 2, 3, 4, and 6 electrodes or sections are shown in Figures 4(a) through 4(e), respectively. The work associated with this contract and this report was concentrated on the simplest switch design, that based on two sections. A four-section switch (presently being worked on with IR&D funds) configuration will result in reduced switch voltages. Switch voltages obtained to date are in excess of 25 V.

As an example, we present here some of the results we obtained with the 0.6328-μm switch. The switch electrodes and guides are shown in Figure 5. The light intensities in the two channels measured at 0.6328 μm wavelength versus the applied voltages are shown in Figure 6. Complete crossover and straight-through states have been achieved with 25- to 30-dB isolation. The variation from sample to sample, we feel, is caused by misalignment of the electrodes with the guide structure. The asymmetry of the switching characteristics with voltage is due mainly to the electrode misalignment and optical damage. Figure 6(a) shows the device operation with the same voltage applied to the split electrodes. The straight-through, =, state is attained in this way. Figure 6(b) shows the device operation in the $\Delta\beta$-reversal mode to attain complete crossover.

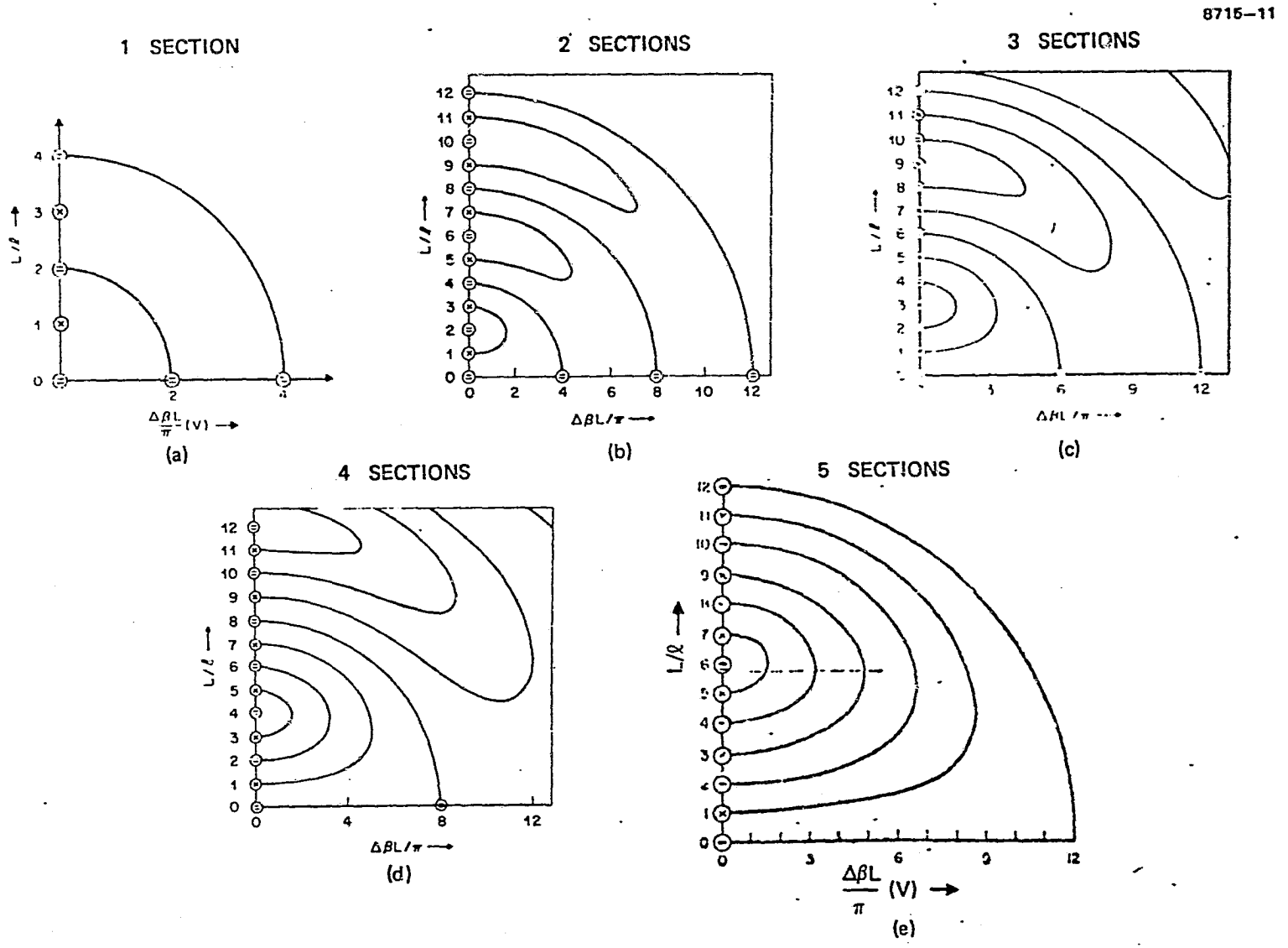

Figure 4. Theoretical switching diagram for 1-, 2-, 3-, 4-, and 6-section switches operating in Δβ reversals.

8499-1

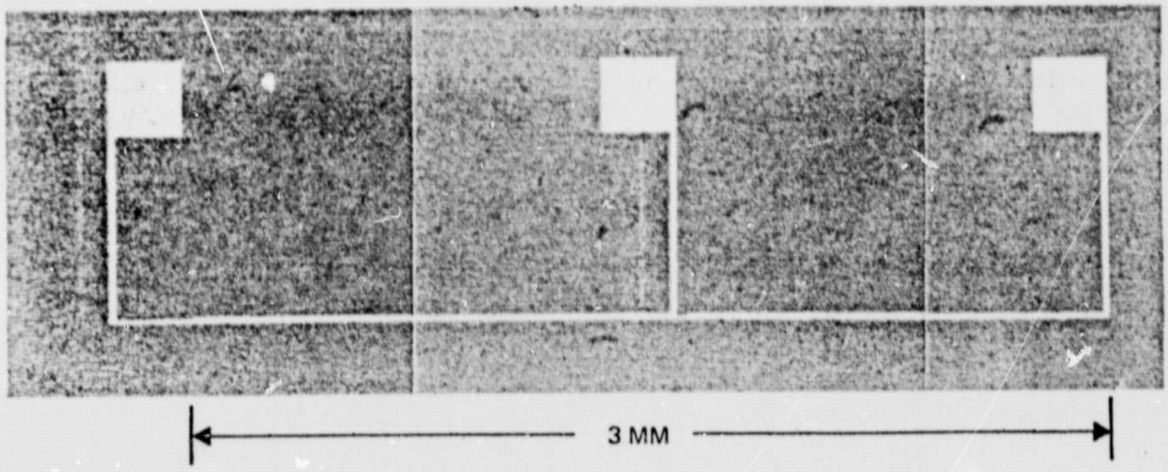

Figure 5. Photograph of the Δβ reversal switch with 3-μm guides. The electrodes are 4 μm wide with 3-μm spacing. The switch length is 3 mm.

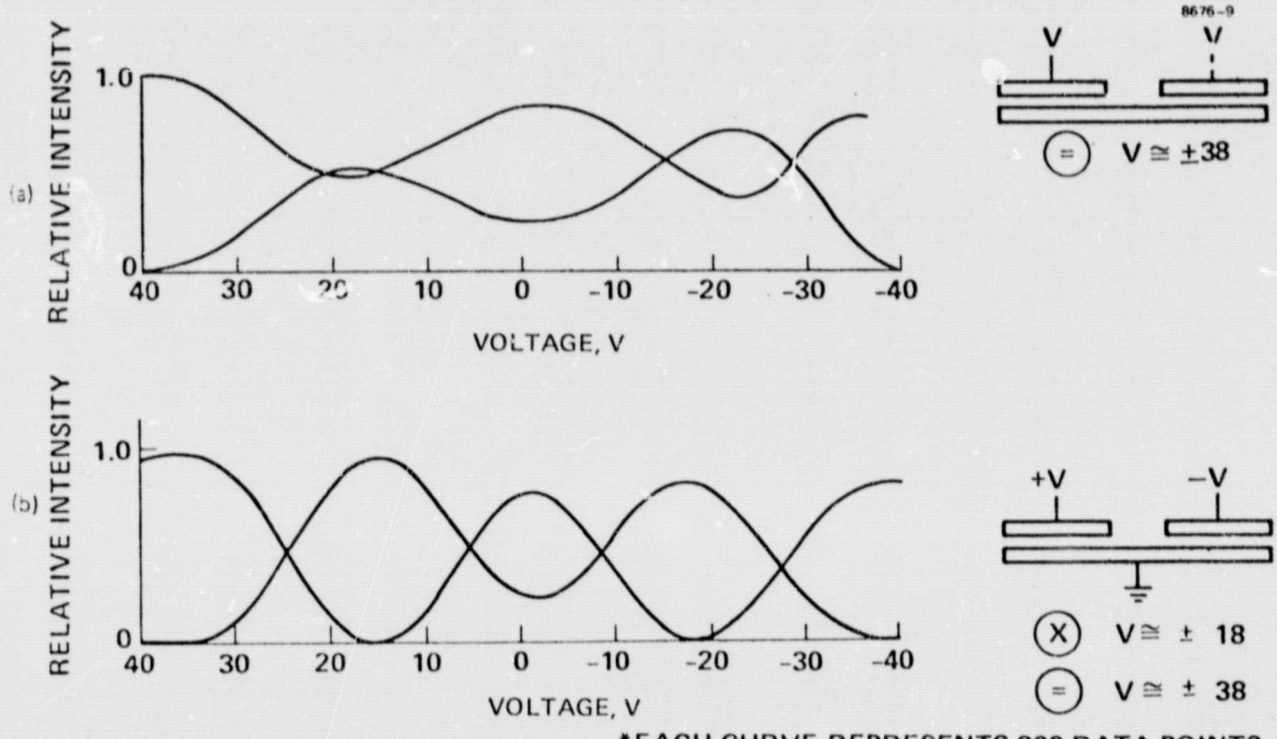

Figure 6. Experimental switch performance in both the (a) conventional and (b) Δβ reversal configurations.

2. Linear Electrooptic (or Pockels) Effect

Electrooptic effects may be broadly defined to include changes in index of refraction, changes in absorption (electro-absorption), and changes in scattering caused by the application of an electric field to a material through which light is propagating. We will mainly discuss refractive index changes induced by electric fields. If the index change varies linearly with the amplitude of the applied field, the effect is known as the linear electrooptic, or Pockels, effect.

As explained by Nye,[3] the Pockels effect is observed only in crystalline solids that lack a center of symmetry. At present, the Pockels effect is the most widely used of the physical effects for constructing light modulators.

The magnitude of the linear electrooptic effect is calculated by using the electrooptic coefficients that relate the changes in refractive index to the amplitude of the applied electric field. The electrooptic coefficients are the elements of a third-rank tensor which interrelates the applied field and light polarization and propagation directions referred to the crystalline axes to the index changes.

Nye[3] gives a detailed description of the meaning and use of the electrooptic tensor. This work is summarized below.

The refractive index of a general crystalline material is specified by the indicatrix or index ellipsoid. The intersection of a plane passing through the center of the index ellipsoid with the ellipsoidal surface is an ellipse. The length B_i of one of the two principal axes of this ellipse is related to the index of refraction n_i of light propagating in a direction normal to the plane and linearly polarized parallel to that principal axis by $n_i = 1/\sqrt{B_i}$. Light propagating normal to the plane but polarized at an angle parallel to neither principal axis propagates as two waves with velocities (refractive indices) corresponding to the reciprocal square roots of the lengths of the two principal axes and with amplitudes proportional to the cosines of the angles between the polarization direction and the direction of the principal axes.

The linear electrooptic effect can be described by small changes in the size and orientation of the indicatrix caused by an applied field. Since the Pockels effect is very small ($\Delta n \lesssim 10^{-4}$), for most purposes rotational effects on the indicatrix can be neglected and the significant changes described through variations in the length of the principal axes of the index ellipsoid.

Crystals that show the linear electrooptic effect are also piezoelectric. Piezoelectricity is an electric-field-induced stress. This is important because stress variations also produce changes in refractive index through the photoelastic effect. Thus, to correctly describe the total index change that takes place when an electric field is applied, it is necessary to prescribe the mechanical constraints placed on the crystal. This is done by specifying the electrooptic coefficients for either the clamped or unclamped conditions. The clamped condition corresponds to a crystal under constant strain and is applicable to situations in which the frequency of the modulating field is well above mechanical crystal resonances. In the unclamped (free) condition, the crystal is under zero stress and the coefficients so specified are used for frequencies well below the mechanical resonances. Thus, generally the clamped coefficients are used for high frequencies and the unclamped coefficients are used for low frequencies.

For linear polarized light propagating perpendicular to a principal plane of the index ellipsoid, the electrooptic refractive index change may be expressed as

$$\Delta n = \frac{-n'^3 r' E}{2} , \tag{9}$$

where n' is a linear combination of the principal refractive indices, r' is a linear sum of electrooptic coefficients, and E is the appropriate component of the applied electric field.

A summary of the use of the electrooptic tensor and tables of electrooptic coefficients were given by Kaminow in Ref. 4.

Because the linear electrooptic effect is basically due to electronic lattice transitions, the response time of the index change approaches the electronic lattice relaxation times, which are in the range 10^{-13} to 10^{-14} sec. Thus, for practical application, the frequency response of the linear electrooptic effect need hardly be considered.

In Table 1 are listed typical values of the electrooptic coefficient and refractive index for $LiNbO_3$, ZnO, and GaAs. These are materials of technological importance which have been used for modulators. Values of Δn calculated from Ref. 4 when a field of 10^4 V/cm is applied are also listed. We note from Table 1 that, even with $LiNbO_3$, which has one of the strongest electrooptic effects of commercially available materials, a field of 10^4 V/cm gives an index change of less than two parts in 10^4.

Table 1. Some Typical Electrooptic Coefficients and Refractive Index Changes for Applied Fields of 10,000 V/cm

Relative Dielectric Constant	Material	λ, μm	n'	r', 10^{-12} m/V	Δn $E = 10^4$ V/cm
28	$LiNbO_3$	0.6328	$2.203(n_\varepsilon)$	$30(r_{33})$	1.6×10^{-4}
12.3	GaAs	0.9	3.6(n)	$1.2(r_{14})$	2.8×10^{-5}
8.2	ZnO	0.6328	$2.015(n_\varepsilon)$	$2.6(r_{33})$	1.1×10^{-5}
Values of n, r, and ε from Ref. 4.					

7128

3. Channel Waveguide Formation in $LiNbO_3$

Low-loss single-mode optical channel waveguides are fabricated in $LiNbO_3$ substrates by the in-diffusion of titanium metal. The presence of Ti ions increases the polarizability of the medium, thus generating a region of higher index of refraction. By adjusting the thickness and

the width of the Ti channel, single-mode optical waveguides in both the transverse and depth directions are easily obtained.

Photolithography techniques are used to define the Ti pattern. These techniques include sputter etching, chemical etching, and photoresist lift-off. At HRL, the photoresist lift-off technique is used to form the desired Ti pattern because it provides a better edge definition of Ti channels. During the fabrication process, the pattern of single-mode channel waveguides are first delineated on the positive Shipley AZ 1305B photoresist. After exposing and developing the photoresist, a 200- to 600-Å-thick Ti film is electron-beam (E-beam) deposited onto the photoresist pattern for guides. The open area is thus filled with Ti metal. The unwanted Ti coating on the photoresist is removed by dissolving the photoresist underneath in acetone. The in-diffusion process is performed in a flowing oxygen atmosphere at a temperature between 900 and 1000°C. The diffusion time is 6 hr. Before diffusion, the Ti metal is oxidized to TiO_2 at 600°C. The addition of the oxidation step before diffusion enhances the surface quality of the sample and the reproducibility of the diffusion process. The temperature cycle is shown in Figure 7.

During E-beam evaporation, the thickness of the Ti film is monitored by a quartz crystal oscillator. After diffusion, waveguide ridges about 2.5 times as high as the original Ti thickness are present. These ridges are used as registration marks in later photolithographic processing.

Typically, we have found that the parameters shown in Table 2 will generate single-mode guides in z-cut $LiNbO_3$ for the TE polarization.

4. Coupling Length between Waveguides

Since there is no analytical description for the modal field of a single diffused channel waveguide, no closed-form expression for the coupling length ℓ is available for directional couplers. However, the coupling between two uniform index channel waveguides has been analyzed.[5] In this case,

$$\ell = \ell_o \exp\left(\frac{d}{\gamma}\right), \tag{10}$$

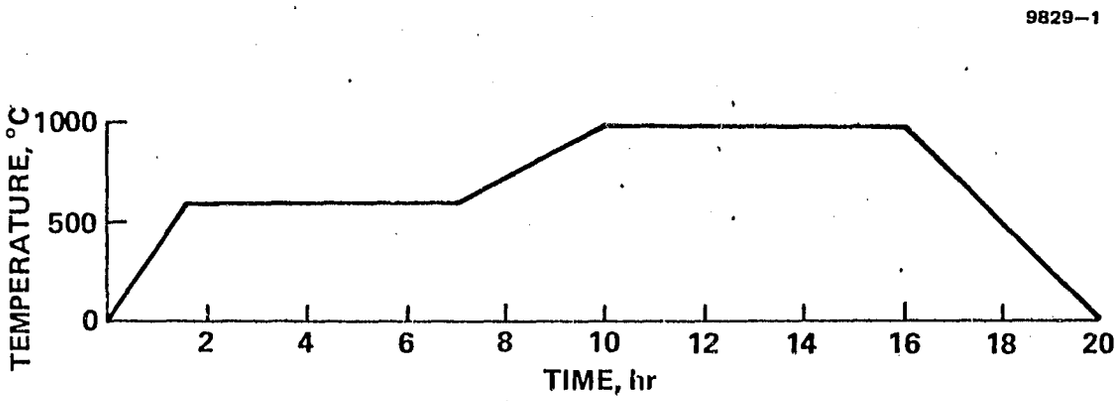

Figure 7. Diffusion temperature cycle for waveguide formation.

Table 2. Single-Mode Diffusion Parameters

λ	Guide Width, μm	Ti Thickness, Å	Diffusion Temperature, °C	Diffusion Time, hr
0.6328	3	200-350	1000	6
0.82	3	400-500	1000	6
0.82	4	350-450	1000	6
1.06	5	470-500	1000	6
1.15	5	570	1000	6

7128

where ℓ_o depends on waveguide parameter but is independent of d, the separation between guides. The quantity γ is the evanescent penetration depth. Qualitatively, ℓ_o depends on the shape of the fields within each guide. For the uniform refractive index channel guides, we can write

$$\ell_o = \frac{\pi\kappa_x \omega\left[1 + \kappa_x^2 \gamma^2\right]}{4 \kappa_z^2 \gamma}, \tag{11}$$

where κ_x is the component of the propagation constant along the direction of separation of the guides, and κ_z is the component along the length of the guides. We have used this theory to predict the general behavior we would expect to see experimentally. Figure 8 shows some of these results.

The coupling length for a particular device geometry is a strong function of wavelength. Figure 8 gives the coupling length versus freespace wavelength for the device geometry in the figure insert. This geometry was chosen to simulate a diffused channel waveguide with a source geometry of two 3-μm-wide stripes of Ti of 3 μm separation on $LiNbO_3$. The curve labelled $\Delta n = 0.005$ gives a coupling length at

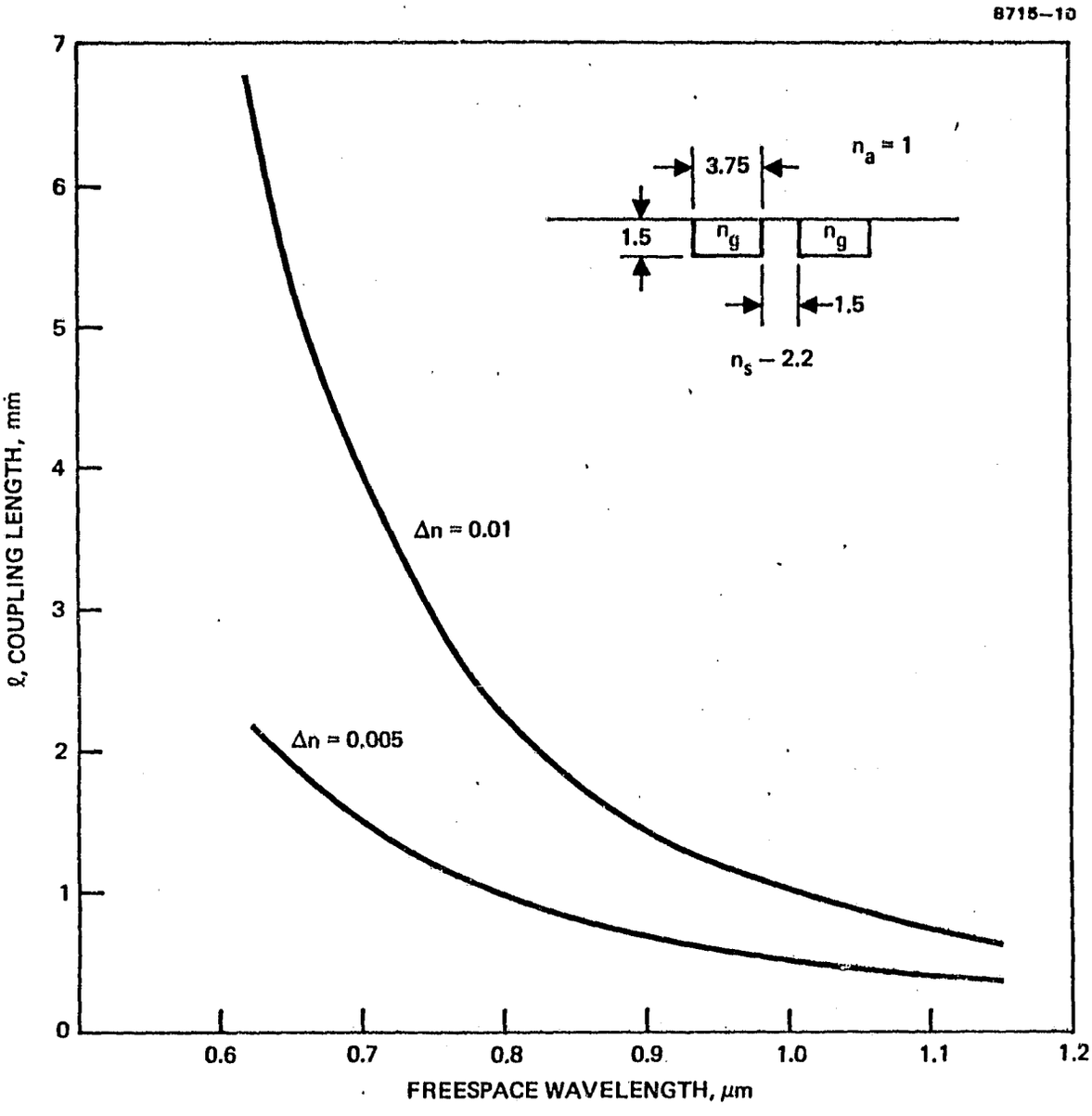

Figure 8. Coupling length versus wavelength for uniform rectangular guides. The index of the superstrate is 1. The substrate has an index of 2.2. The guide index is 2.2 + Δn. The guide dimensions are shown in the insert.

0.6328 μm corresponding to the experimental results for 300 Å of Ti (i.e., $\ell \simeq 2$ mm). The other curve gives the Δn required to give an $\ell \simeq 2$ mm at 0.82 μm.

Recent articles by Schmidt et al.[6] have contained experimental data for the coupling length for various guide configurations and wavelengths. These data are shown in Figure 9. For d = 3 μm, the following Ti thicknesses and waveguide widths produce an $\ell \simeq 2$ mm:

λ, μm	Ti Thickness, Å	W, μm
0.6328	300	3
0.83	400	4
1.06	460	5

5. Frequency Response

The bandwidth of the present Δβ reversal switch has been estimated assuming a 50-Ω system. In this case, the bandwidth is mainly limited by the capacitance. For the electrode pattern shown in Figure 10(a), the capacitance has been calculated and is plotted in Figure 10(b). With $\alpha = 0.57$, this configuration is exactly that of our switch pattern. For a length of 3 mm, the capacitance is 1.92 pF. The bandwidth is calculated to be

$$\Delta f = \frac{1}{2\pi RC} = 1.66 \text{ GHz} . \tag{12}$$

The drive power required to operate the switch as a modulator from the 50/50 bias point may be expressed as

$$P = V_{in}^2/2R , \tag{13}$$

where V_{in} is one-half of the peak drive voltage required for switching from a crossed state to a parallel state, and R is the resistance of

9829–17

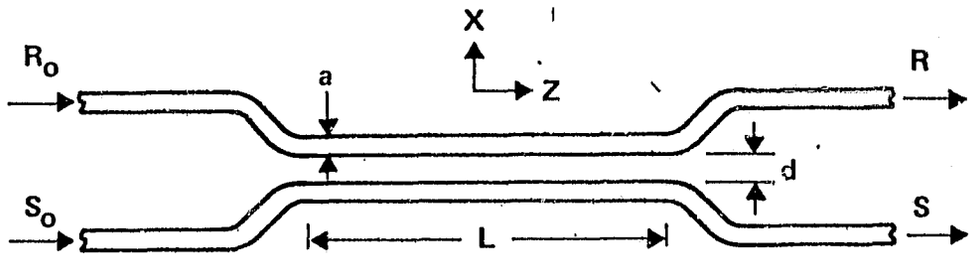

Figure 9(a). Top view of a waveguide directional coupler where L is the coupler length, a is the waveguide width, and d is the separation between the waveguides in the interaction region.

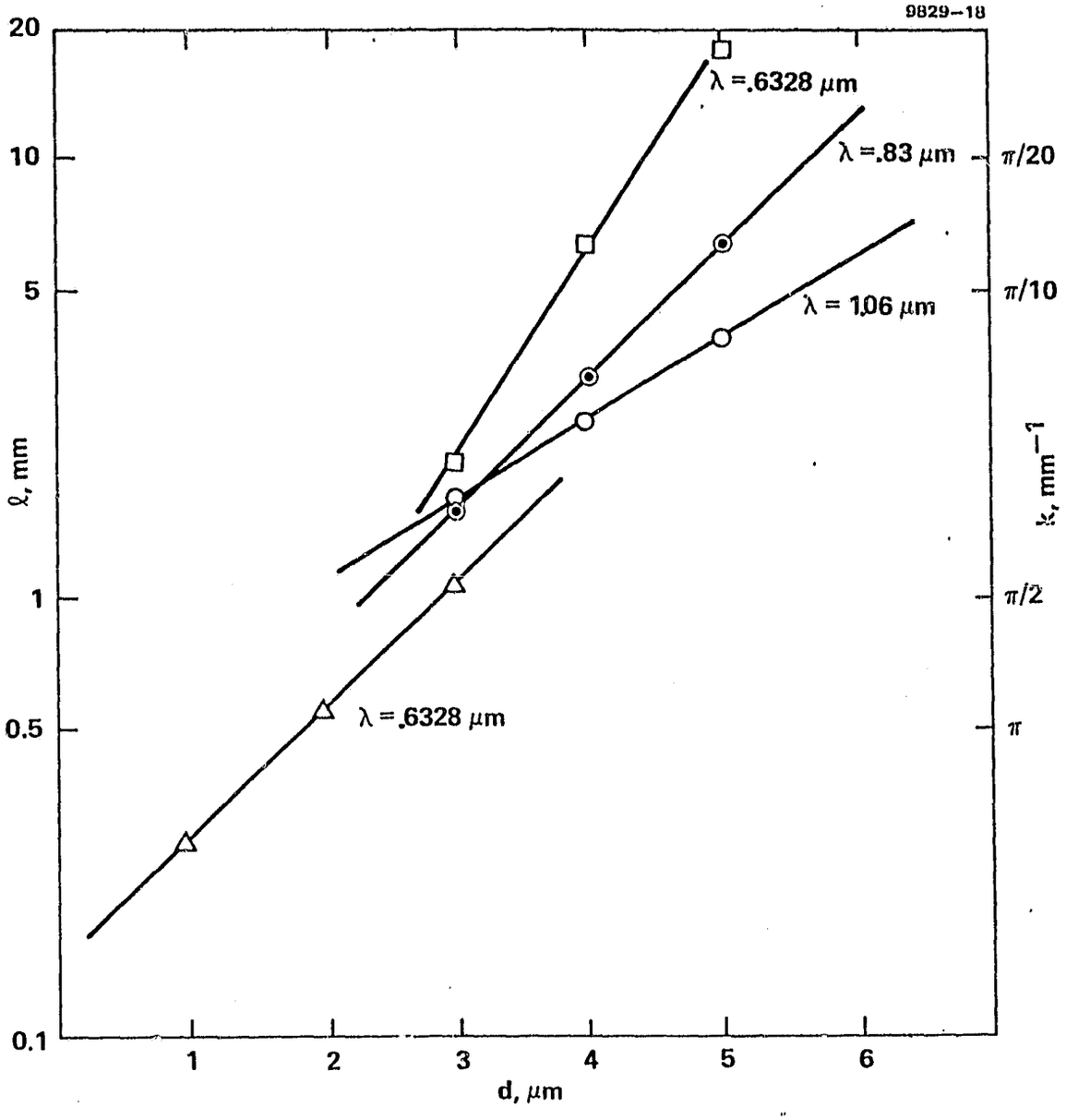

Figure 9(b). Coupling coefficient of Ti-diffused $LiNbO_3$ waveguides at 1.06-, 0.83-, and 0.633-μm wavelegnths as a function of waveguide separation. For each wavelength, the waveguides were fabricated so as to be single mode using the following fabrication parameters: (□) λ = 0.6328 μm, τ (Ti metal thickness) = 300 Å, a = 3 μm; (Δ) λ = 0.6328 μm, τ = 300 Å, a = 2 μm; (◉) λ = 0.83 μm, τ = 400 Å, a = 4 μm; and (○) λ = 1.06 μm, τ = 460 Å, a = 5 μm.

the system. Using Eq. 14, the figure of merit, or power per bandwidth, is given by

$$P/B = \pi/4 \; C \; V_m^2 \quad . \tag{14}$$

For our present device, this is ∿0.122 mW/MHz.

8. Phase Shifter Design and Performance

The phase shifter is used to allow quadrature detection of the gyro-induced phase shifter. Kaminow et al.[7] have reported results of a similar modulator in Y-cut $LiNbO_3$.

Our phase shifter consists of a channel waveguide and two aluminum electrodes in a configuration in which the electric vector of a TE wave excited in the waveguide and the modulating field applied to the electrodes are perpendicular in a Z-cut $LiNbO_3$ sample. The modulating electric field E_3 produces a change in the refractive index of $\Delta n = n^3 \, r_{13} \, E_3/2$, where r_{13} is the appropriate electrooptic coefficient. In response to this index change, the light beam suffers a phase retardation of $\Delta\theta = 2\pi L \Delta n/\lambda$ in the waveguide, where L_p is the length of the channel waveguide.

Many electrode patterns are possible for this application. An evaluation of the phase shifter performance in radians per volt can be obtained using data taken from the switching characteristic. From Eq. 5, the condition required for a parallel state is given by

$$(KL_p)^2 + (2\delta)^2 = (4\pi)^2 \tag{15}$$

or

$$\delta = \frac{2\pi}{\lambda} \Delta n = \sqrt{\frac{(2\pi)^2 - (KL_p)^2}{L_p^2}} \quad . \tag{16}$$

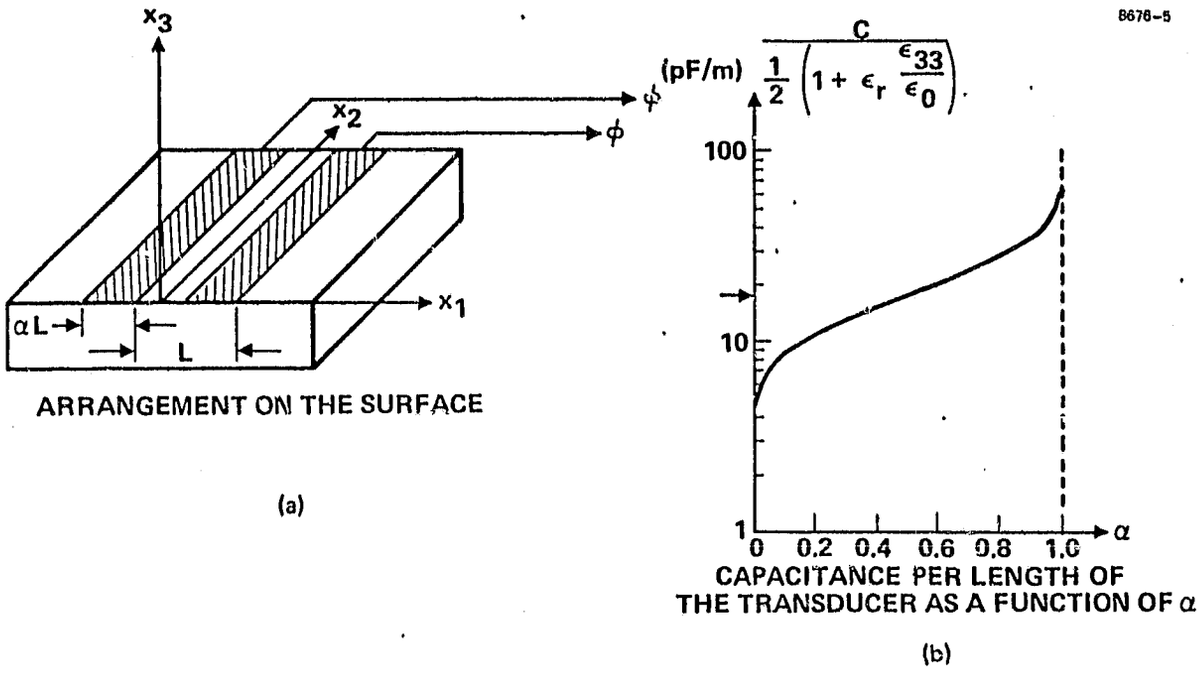

Figure 10. Electrode configuration used in Δβ reversal switch and the calculated electrode capacitance.

Our 0.6328 μm device is 3 mm long, which is also ∿2ℓ; hence, at a voltage of 36 V, corresponding to a parallel state, δ is ∿2 rad/mm. Since δ is proportional to the applied voltage V:

$$\delta(V) = 0.05\ V\ \text{rad/mm} . \qquad (17)$$

For this electrode configuration, of length 1.5 mm, we have measured the phase shift by using the experimental arrangement of Figure 11(a). The interference of the two (phase shifted and non-shifted) beams produces interference fringes. The position of these fringes is dependent on the phase shift or applied voltage. Figure 11(b) shows the signal applied to the phase shifter and the corresponding intensity through a pin hole at the fringe patterns. This signal corresponds to an approximate π phase shift for an applied 26-V, or 0.12 rad/V, shift; the calculated shift was 0.15 rad/V.

B. FIBER ATTACHMENT

1. Coupling Apparatus

We had proposed to use the fiber attachment technique illustrated in Figure 12. To hold the ITT single-mode fibers, V-grooves (Figure 13(a)) were to be etched in <100>-oriented Si wafers with KOH. With this technique, the groove widths are such that the fiber core is just above the Si surface (Figure 13(b)), and the photolithographic masks have matching groove and guide center-to-center spacings. But we found that, when the $LiNbO_3$ chip is flipped and placed on the Si surface, the fibers and channel guides cannot be easily aligned. This is particularly true of the output pair of fibers.

It proved to be very difficult with this technique to obtain optimum coupling from the fiber through the chip to the other fiber. This is primarily because both sides must be realigned on small rotations of the chip and because the visual alignments available are not adequate to position the guides exactly in the center of the V grooves. These difficulties forced us to develop a new technique for fiber attachment.

8676 4

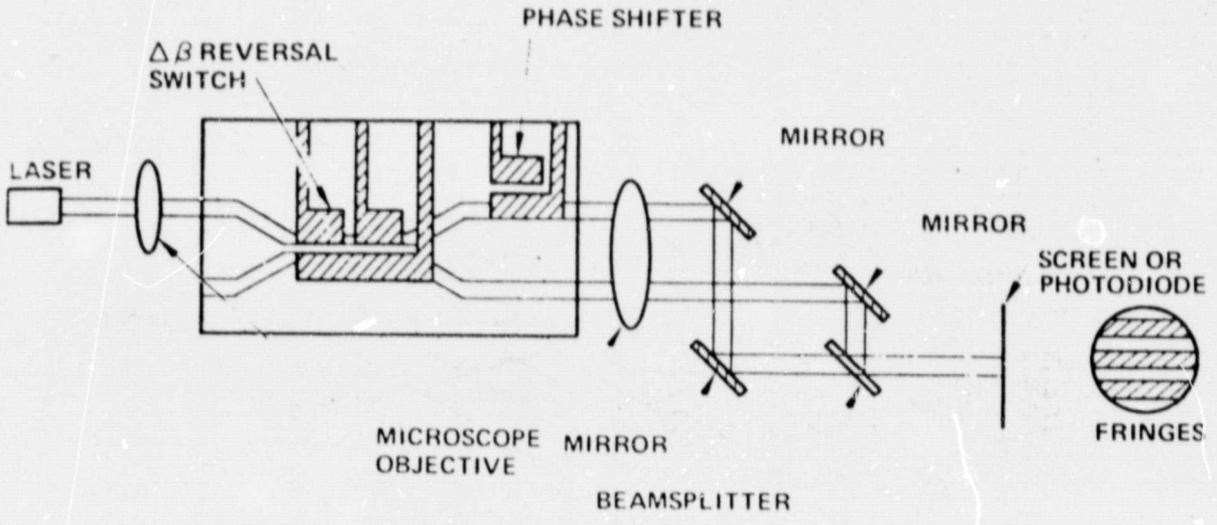

- REVERSAL SWITCH ADJUSTED FOR 50/50 SPLIT
- FRINGES SHIFT AS PHASE IS VARIED BY APPLICATION OF VOLTAGE

(a)

8676–2

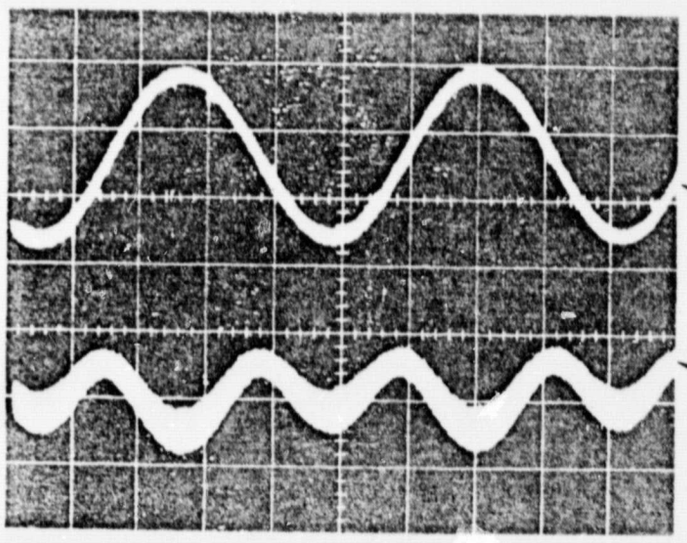

SHOWN IS AN APPROXIMATE π PHASE SHIFT FOR AN APPLIED VOLTAGE OF 26 VOLTS OR 0.12 RADIAN/VOLT (PREDICTED 0.15 RADIAN/VOLT)

(b)

Figure 11. (a) Phase shifter experimental test configuration.
(b) Phase shifter test results.

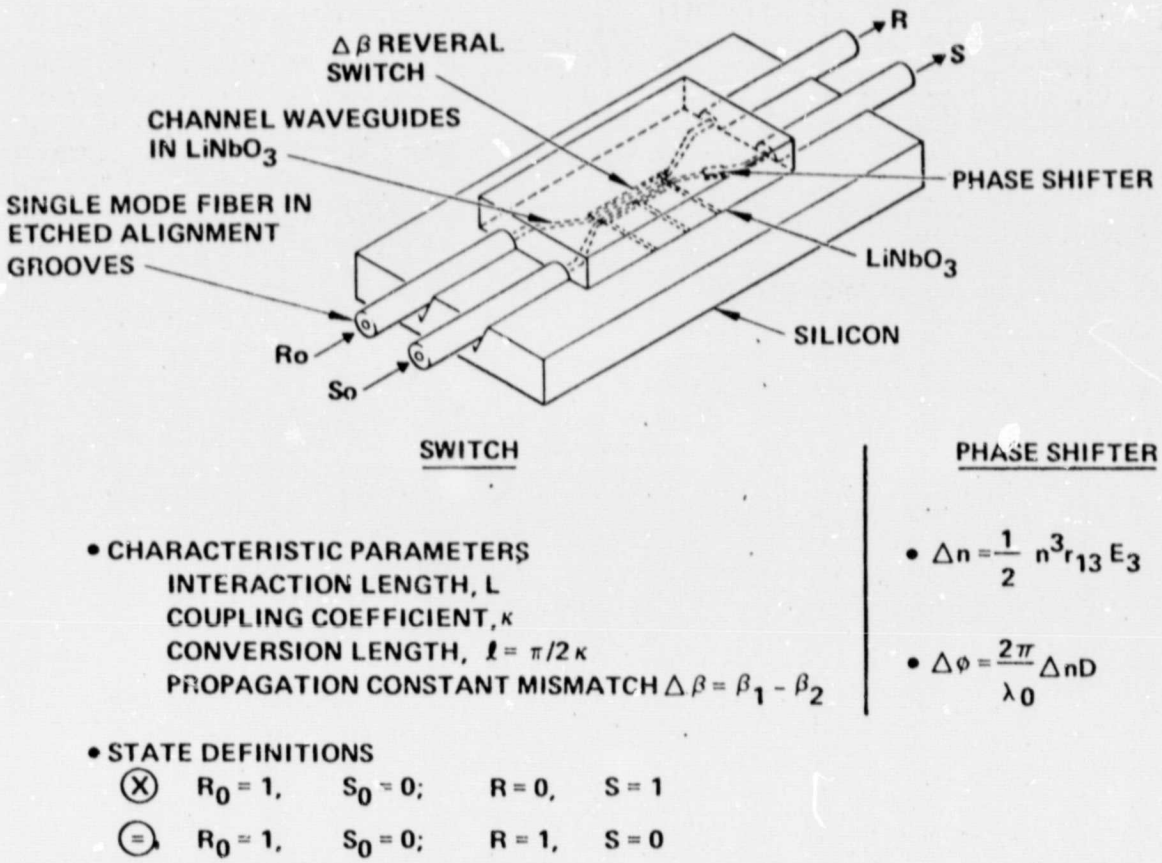

Figure 12. Schematic of the four-port optical switch module.

8676-8

- MATERIAL – (100) SILICON
- ETCHANT – KOH

(a)

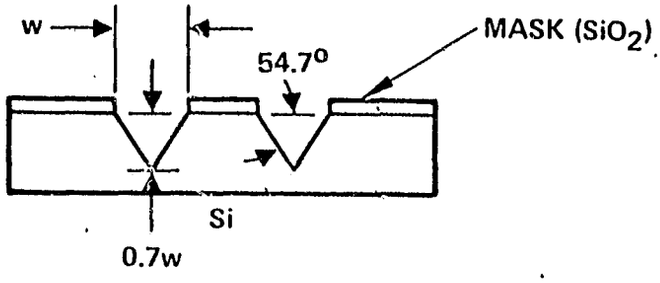

- DESIRED FIBER GROOVES

(b)

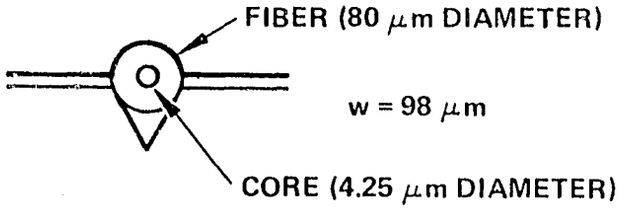

- DESIRED ADJUSTMENT GROOVES
  w = 211 μm

Figure 13. In (100)-oriented silicon wafers, V grooves can be etched with KOH. The dimensions of these grooves are shown in (a). The desired configuration for our fiber is shown in (b).

This new technique is illustrated in Figure 14. The V-groove technology is again used to establish the fiber-to-fiber separation, but a separate Si chip is used on each face of the $LiNbO_3$ sample. After the fibers are positioned in the grooves, the Si and fibers are polished such that the fiber and Si edge are aligned (see Figure 15). The first two (input) fibers can then be aligned and fixed into place before the second is aligned. In addition, the sample face is not flipped down on the Si surface, thus making electrical connection easier.

The fixing is done with the epoxy, and an adjustment is available for the fiber position normal to the surface plane after fixing. This is done by flexing the Si wafer with a set screw. The lowest loss observed to date for fiber-to-chip coupling was ∿3.7 dB. We are still conducting experiments to isolate the problems so that the losses can be reduced to the theoretical value of ∿1.5 dB (see Section 3). The problem is related to the surface preparation, an excess loss due to the fiber being epoxied into the V-grooves, or alignment. The fiber-to-chip coupling clearly needs improvement; a more in-depth discussion of the experiments being conducted in this area is deferred to Section 4.

2. Fiber-to-Channel Coupling Performance Expectations

The coupling between a fiber and channel waveguide has been described by Hocker and Burns.[8] Their approach is to describe the mode of the channel waveguide by a rectangular Gaussian beam with waists in beam half widths of W_x and W_y. The HE_{11} mode of the fiber can be approximated by a circular Gaussian with waist a. Cohen[9] has shown that the coupling coefficient between rectangular and circular Gaussians is an optimum at the waist of the two beams and is given by

$$K = \frac{4}{\left(\frac{W_x}{a} + \frac{a}{W_x}\right)\left(\frac{W_y}{a} + \frac{a}{W_y}\right)} \quad . \tag{18}$$

M13359

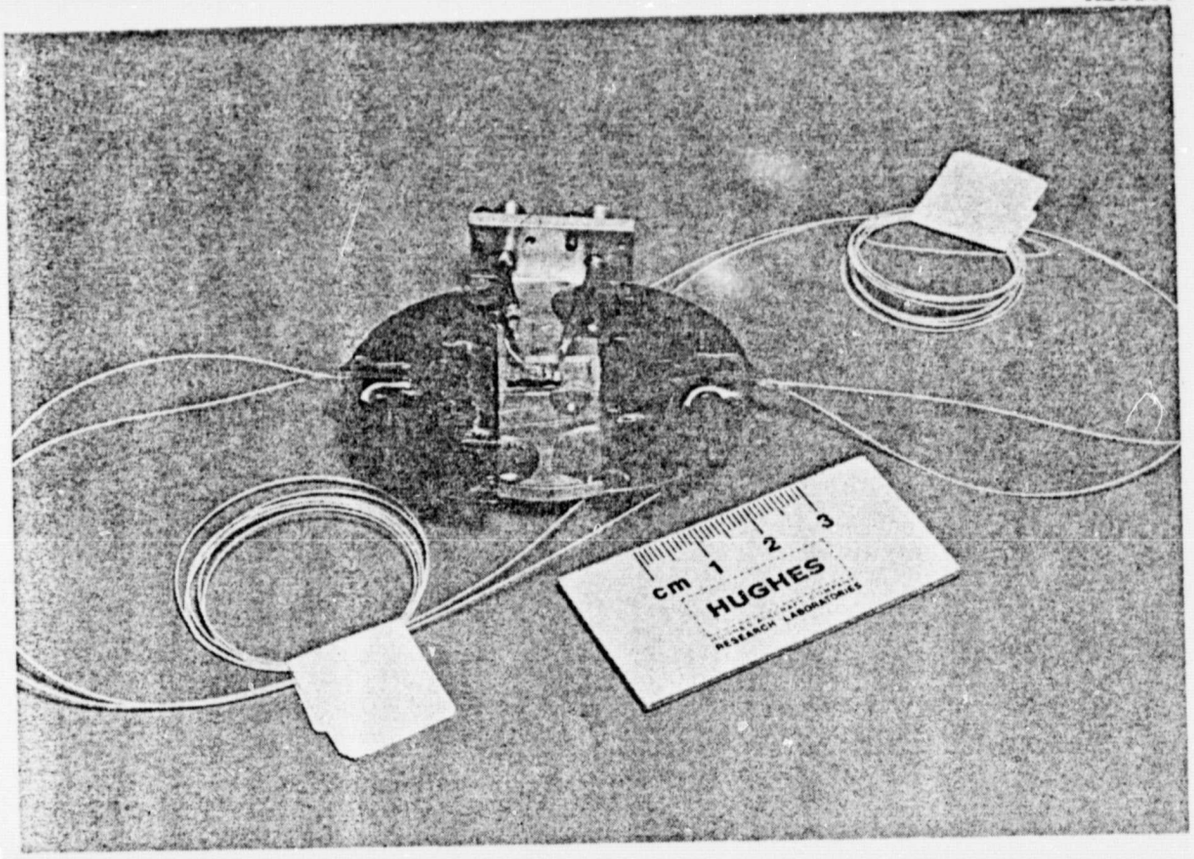

Figure 14. Photograph of fiber-optic switch with attached pigtails.

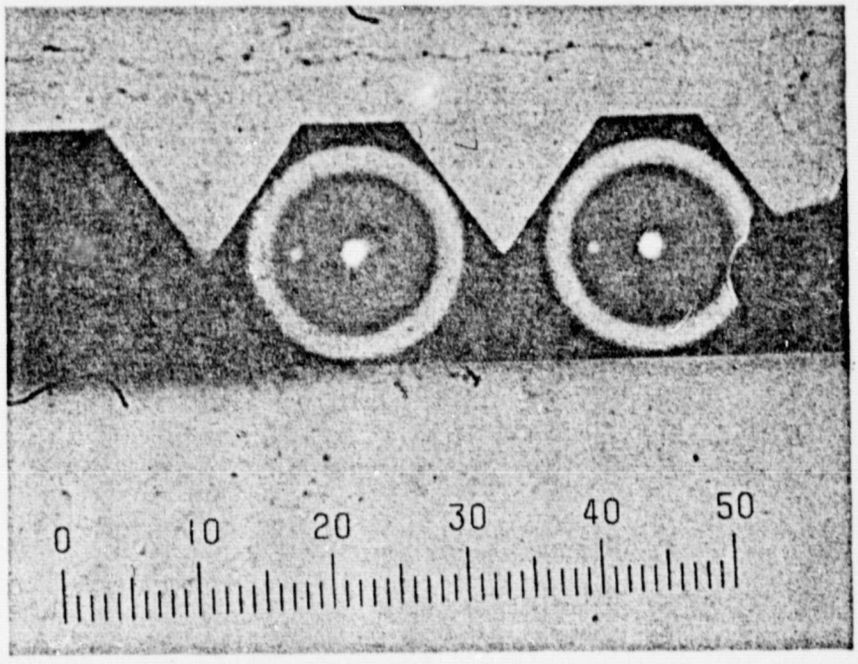

Figure 15. Photograph of the polished end of Si wafer with V grooves containing single mode fibers.

The total coupling from fiber to channel is then given by

$$K' = T\, I_x^2\, I_y^2\, I_2^4\, K \quad , \tag{19}$$

where T is the transmissivity, I_x is the overlap of channel mode in the x direction and a Gaussian of waist W_x, I_y is the overlap of channel mode in the y direction and a Gaussian of waist W_y, and I_2 is the overlap of the HE_{11} mode of the fiber and a circular Gaussian of waist a. The value of I_x, I_y, and I_2 were shown to be on the order of 0.98. Hocker and Burns also showed that K' is optimum for $(W_x\, W_y)^{1/2} = a$.

For long diffusion times as compared with the time required to diffuse all the source material from the surface into the bulk, the index profile for a strip of infinite extent in the z direction and extending from x = -W/2 to x = W/2 in the x direction is (the substrate occupies the space y > 0)

$$n^2(x,y) = n_b^2 + \left(n_s^2 - n_b^2\right) f(y/D)\; g(2x/W) \tag{20}$$

$$f(y/D) = \exp\,(-y^2/D^2) \tag{21}$$

$$g(2x/W) = \frac{1}{2}\left\{\operatorname{erf}\left[(W/2D)\;(1 + 2x/W) + \operatorname{erf}\;\;(W/2D)\;(1 - 2x/W)\right]\right\} . \tag{22}$$

Because of lateral diffusion, the geometrical aspect ratio of the guide is not W/D, but is defined as $2x_{1/2}/D$, where

$$g\left(\frac{2x_{1/2}}{W}\right) = \frac{1}{2}\, g(0) \quad . \tag{23}$$

The geometrical aspect ratio is plotted in Figure 16 versus the quantity W/D. For a given W and increasing D (increased diffusion time or temperature), the geometrical aspect ratio decreases to ∿1.7 for W = D and

remains constant at this value. According to the calculations of Hocker and Burns, this corresponds to the maximum coupling, although, as can be seen from Figure 17(b), the decrease with increasing $2x_{1/2}/D$ is slow. These calculations are based on the solid curve in Figure 17(a), which is a fit to calculated data for typical diffusion profiles and effective index of the guides determinable from b_0. The data show that approximately 80% coupling may be achieved if all parameters are optimized in a single diffusion; this corresponds to 64% throughput from fiber to fiber if the propagation and bend losses are neglected (64% corresponds to ∿2 dB loss).

Mode profiles for the 4 μm waveguide with 420 Å of Ti are shown in Figure 18. These profiles yield an estimated coupling coefficient k' of ∿0.7, which gives a loss of ∿1.5 dB. When this theoretical value is achieved, the throughput loss of the waveguide device will be 5 dB or less (∿2 dB chip loss).

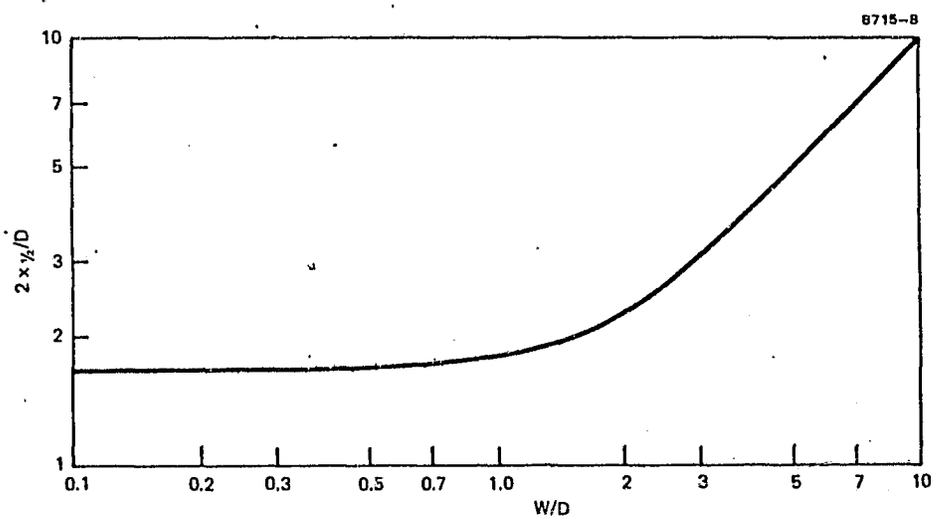

Figure 16. The geometric aspect ratio of an isotropically diffused channel waveguide plotted versus the ratio of the undiffused channel width W to the diffusion length D.

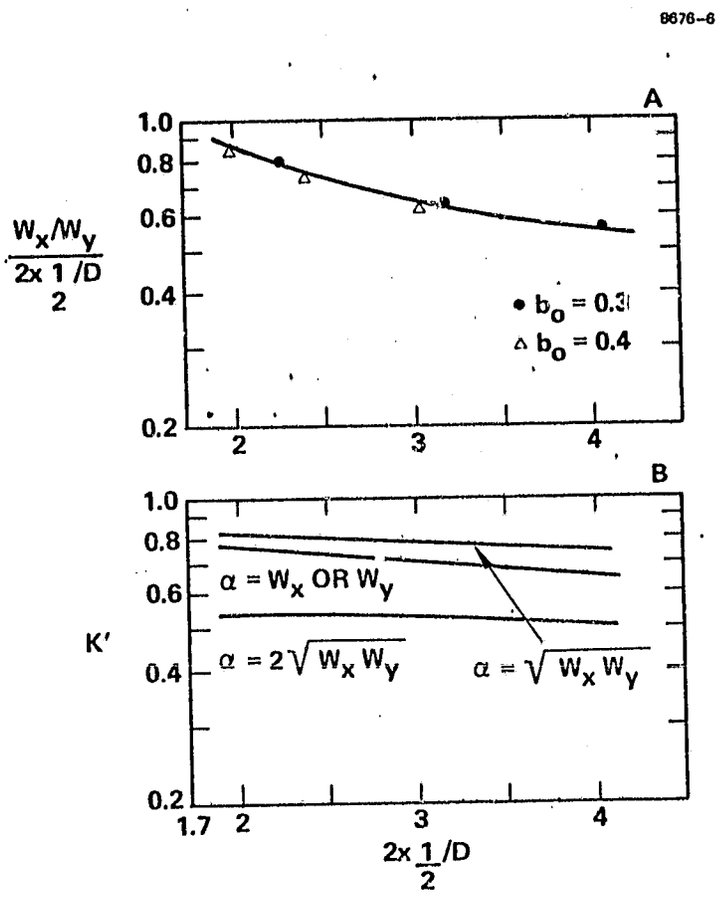

Figure 17.
Plotted in (a) is the ratio of the modal aspect ratios to the geometric aspect ratio for the first-order mode in several diffused channel waveguides. In (b) is the power coupling coefficient for end fire coupling between a circular fiber with mode radius a and a diffused channel waveguide with mode half widths W_x and W_y. Both quantities are plotted versus the geometric aspect ratio of the diffused channel waveguide. After Hocker and Burns.

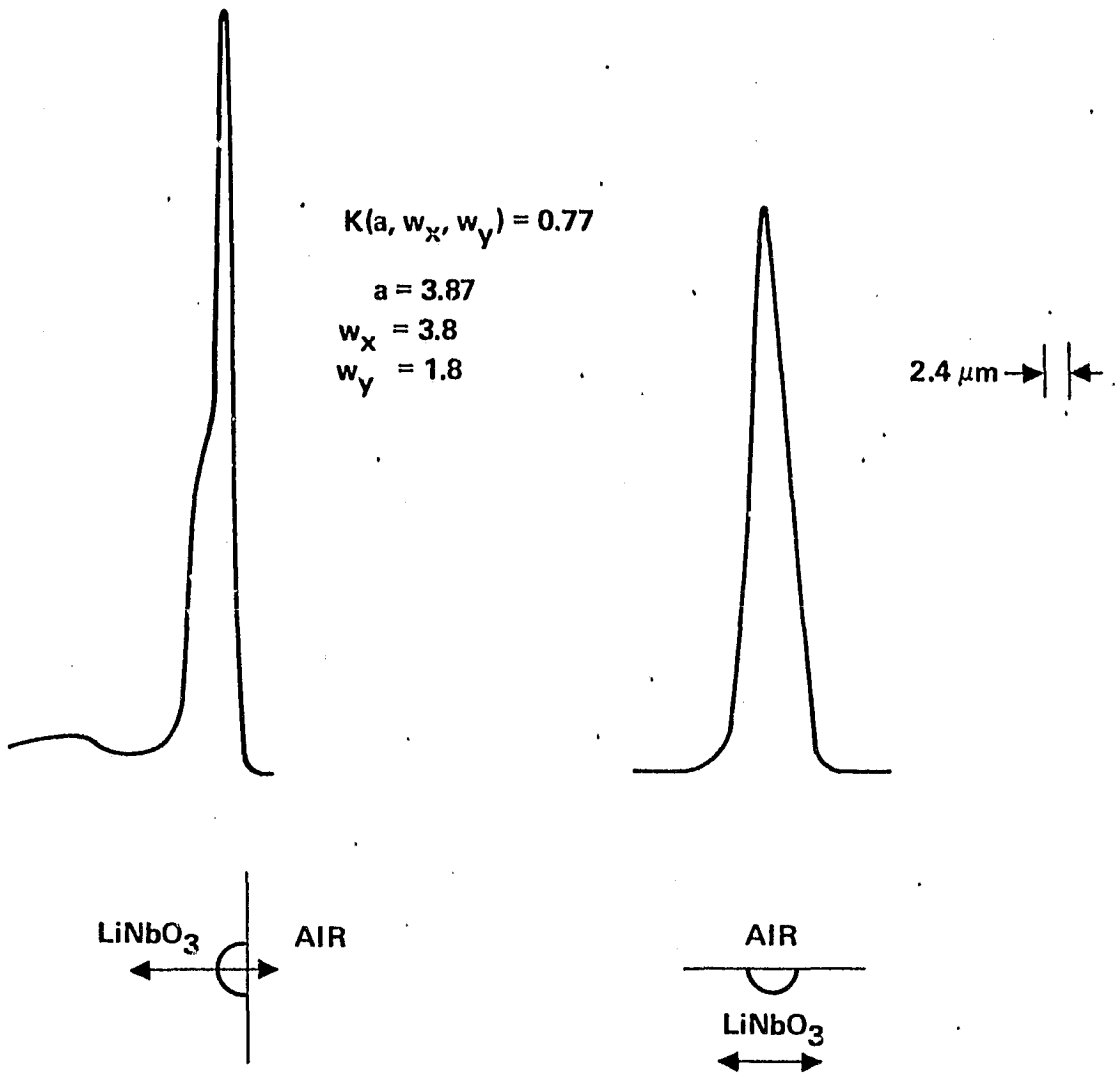

Figure 18. Mode profile as measured for a single mode channel diffused from a 4-μm-wide source of 420-Å-thick Ti.

SECTION 3

SWITCH AND CHIP PERFORMANCE AT 0.85 μm

A. INTRODUCTION

During this program, we were to design and fabricate devices consisting of an electrically activated channel waveguide 2 x 2 switch, a channel waveguide phase shifter, and attached pigtails. The theory and predicated device performance are discussed in Section 2. This section presents the performance of the 0.85-μm devices and presents some of the problems encountered during device fabrication and testing.

B. SWITCH AND PHASE SHIFTER FABRICATION

The 0.85-μm switches were fabricated using 4-μm-wide, 420-Å-thick sources of Ti by diffusion at 1000°C for 6 hours. Waveguide formation in $LiNbO_3$ is discussed in Section 2. The mask used to define the Ti sources is schematically drawn in Figure 19; the dimensions are those of the actual mask. The electrodes are those shown in Figure 5.

Two versions of these chips were fabricated and delivered (two each of each version). The first version had the electrodes placed directly on the $LiNbO_3$ waveguides as required for the z-cut $LiNbO_3$ switch. This metal is a source of propagation loss (∿1 dB/mm for TE mode and >10 dB/mm for TM). Therefore, it is desirable (and in fact necessary for low-loss chips) to isolate the electrodes from the $LiNbO_3$ surface with a low-loss dielectric if the z-cut configuration is to be used. This isolation reduces the propagation losses for both polarizations, making is possible to switch the TM polarization with the r_{33} electrooptic coefficient. Such an isolation layer was fabricated for the second version of this chip. A 1000-Å layer of SiO_2 was deposited on the $LiNbO_3$ chip prior to electrode fabrication.

1. Version I — Results

These samples have no buffer layer between the electrodes and the waveguides; therefore, the guides propagate with reasonable loss only the

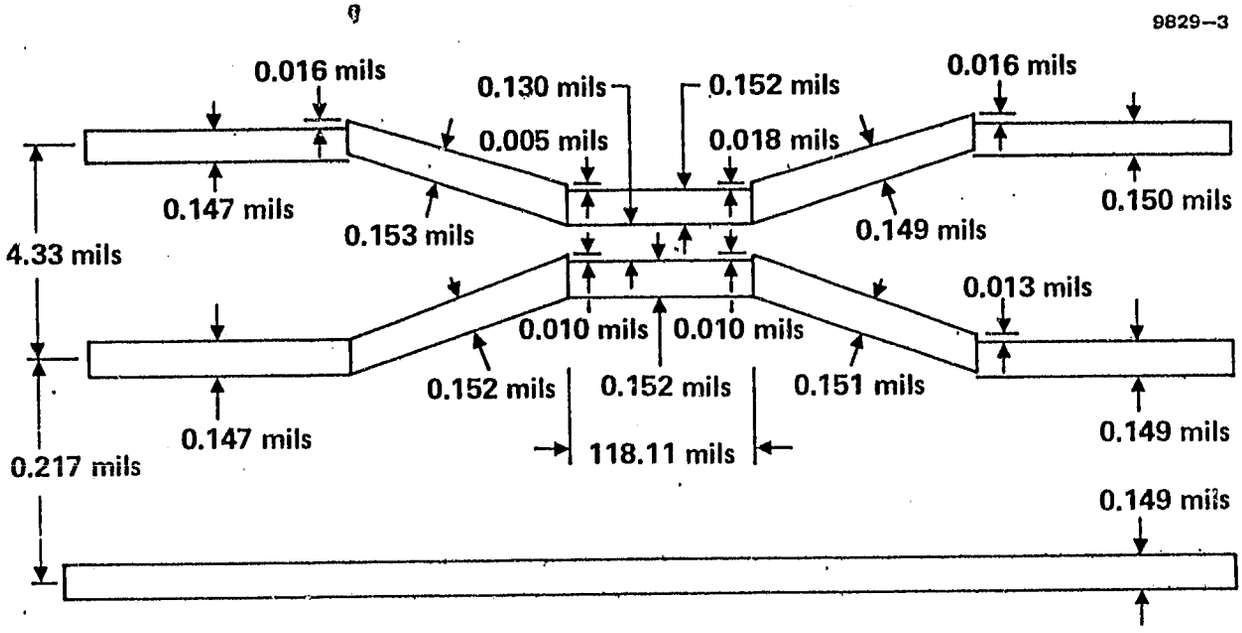

Figure 19. Schematic of actual waveguide mask used for the JPL switch program.

TE polarization. The results given here are with the fiber pigtails in place and represent the performance of the total chip. These chips have serial numbers 2 and 6.

The switch characteristics for these chips with one port excited are given in Figure 20 (a) and (b). Device #6 has an obvious loss on one port that does not exist on the other port. This loss is believed to be in the fiber-to-chip coupler. The total losses for these two chips are 11 dB and 20 dB (average) for chips 2 and 6, respectively.

A crosstalk-versus-time measurement was made using chip #2 at the cross state. These data are shown in Figure 21. An initial crosstalk of -35 dB decayed to ∿-27 dB in ∿5 min, indicating a relatively long relaxation time.

A second measurement of drift in the optical intensity in a channel was made versus modulation frequency. The experimental setup for this measurement is shown inFigure 22(a). A dc bias offset was applied from the function generator to maximize the optical modulation. The modulation signal was sinusoidal with a peak-to-peak amplitude of 10 V. The total optical power from the fiber was ∿10 μW. The interest here was to measure the frequency dependence of the hystereses and not the absolute amplitude; hence, only relative amplitudes are plotted. No measurement was made of the optical modulation depth. If any hystersis exists in the modulation, it will be displayed on the scope. An example of this hysteresis is shown inFigure 22(b). The width of this modulation hysteresis has been measured and plotted versus frequency. These data are shown in Figure 23. There is an apparent break point at about 2500 Hz.

No phase shifter was tested on these samples.

2. Version II — Results

Because of time and equipment limitations, only one sample (#4) was tested in any detail. These samples have the buffer layer between the electrodes and waveguides. Both polarizations propagate through the

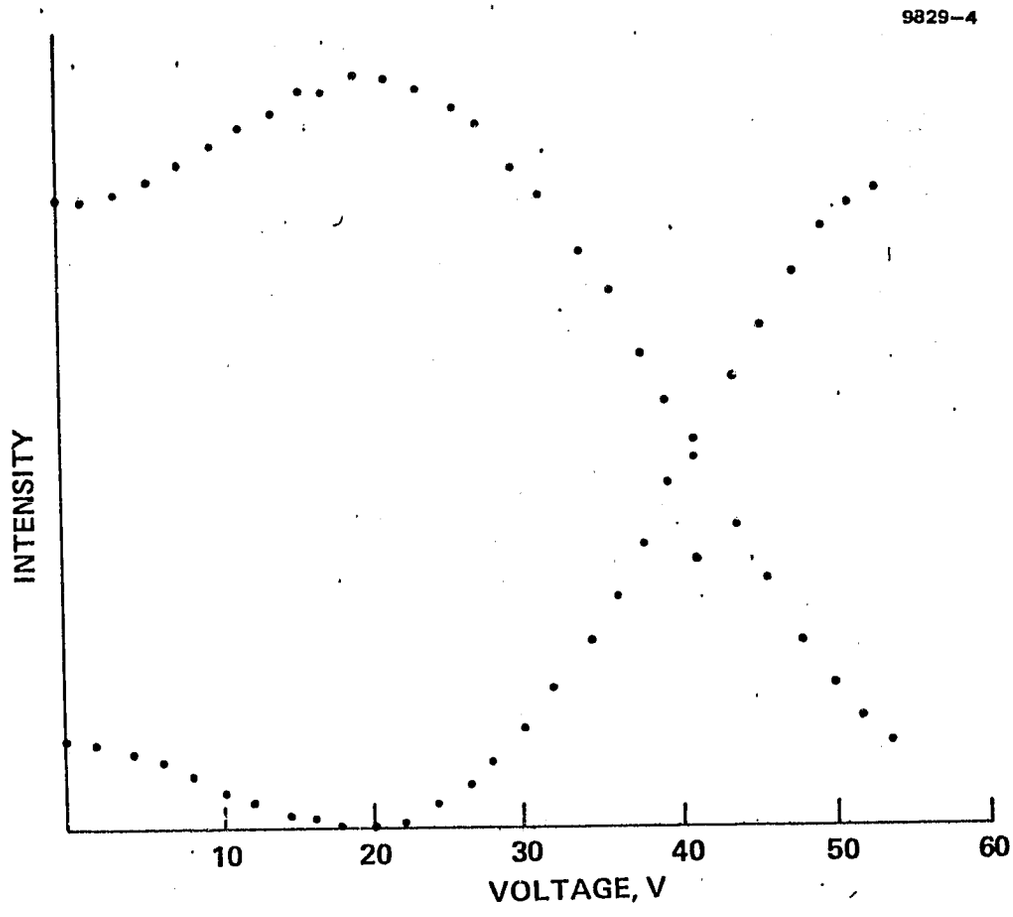

Figure 20(a). Sample #2 $\Delta\beta$ reversal switch characteristic.

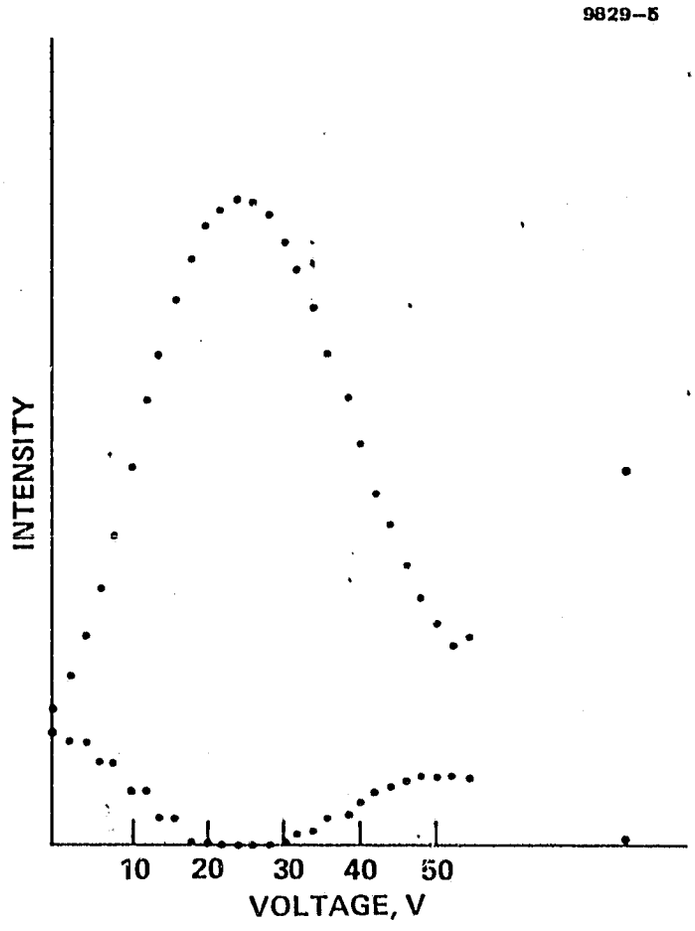

Figure 20(b).
Sample #6 $\Delta\beta$ reversal switch characteristic.

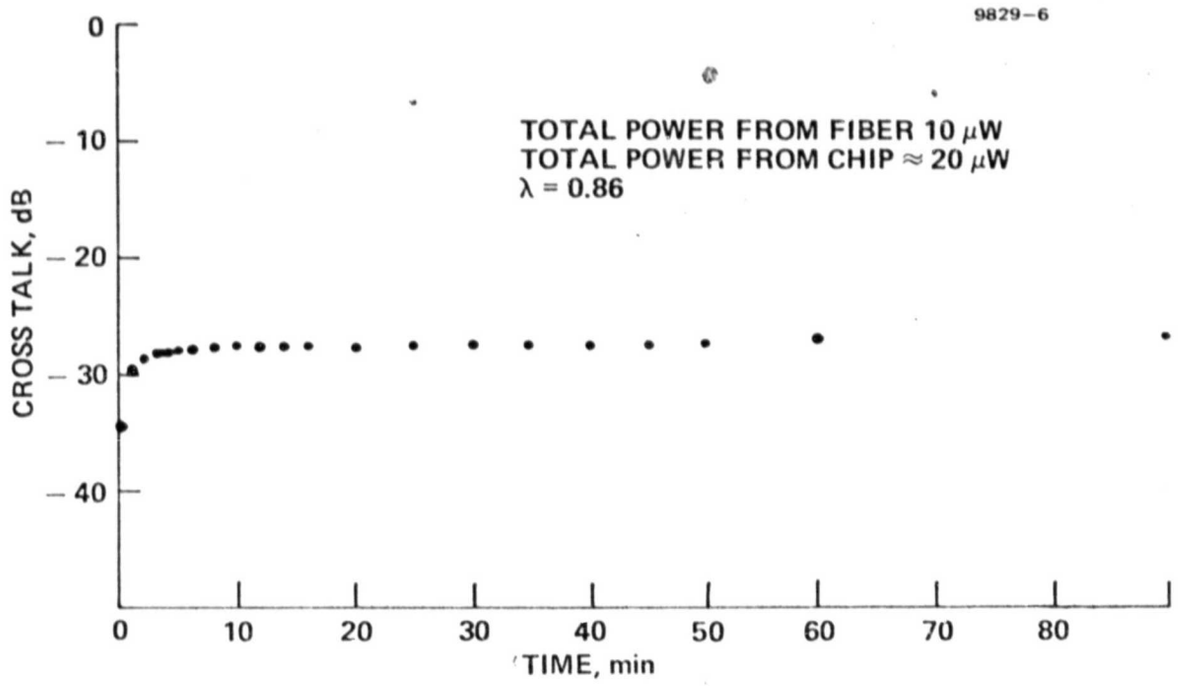

Figure 21. Crosstalk versus time for the cross state of sample #2.

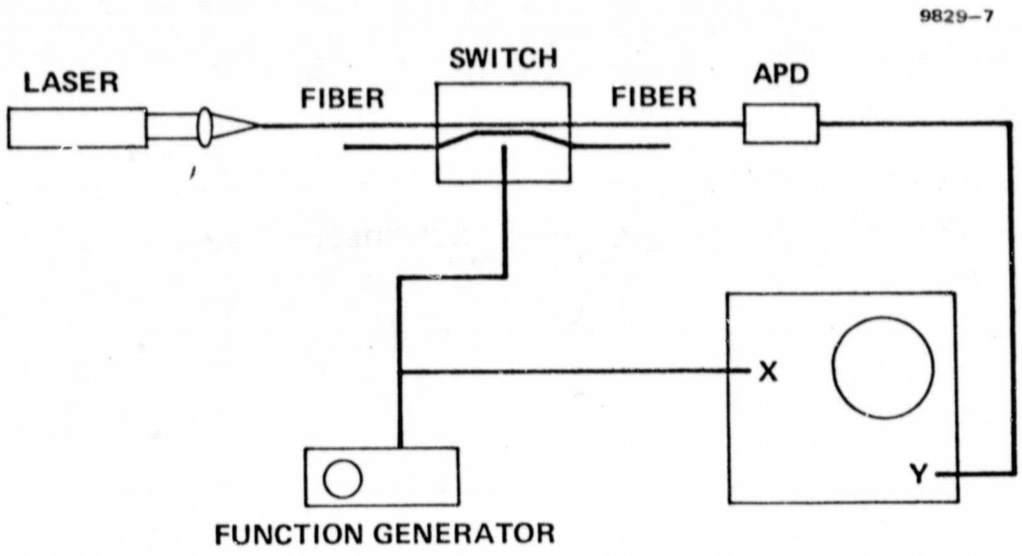

Figure 22(a). Experimental step up for measuring the modulation hysteresis.

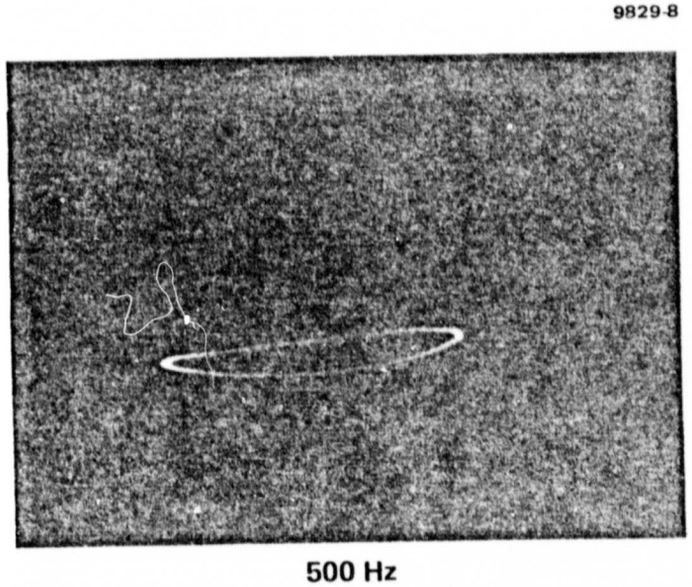

Figure 22(b).
Example hysteresis pattern from oscilloscope.

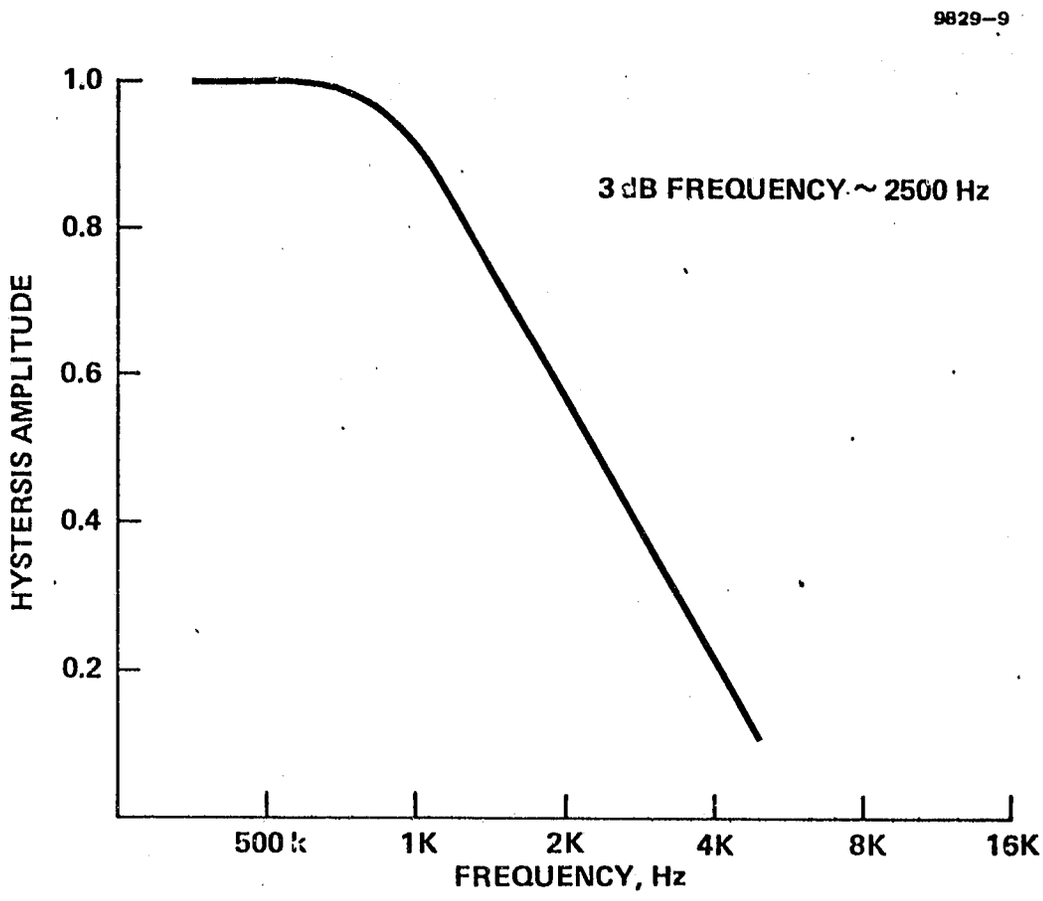

Figure 23. Hysteresis amplitude versus frequency for sample #2.

sample with approximately the same loss. This fact indicates that the SiO_2 layer has isolated the modes from the electrodes, thus reducing the propagation losses. However, the overall losses of the completed devices have not been significantly reduced. The losses for devices #4 and #5 are ∿14 and ∿20 dB, respectively.

Optical intensity versus voltage in the two channels of device #4 are shown in Figure 24 for both the conventional and reversal configurations. The high crosstalk level is due to the presence of both polarizations. The lower apparent switch voltage versus the Version I devices is due to the propagation of primarily the TM polarization. This polarization takes advantage of the r_{33} electrooptic coefficient, which is approximately three times larger than r_{13}.

On device #4, the phase shifter was tested. The experimental configuration is schematically illustrated in Figure 25. The test result, shown in Figure 26, shows in excess of a π phase shift with 15 V applied. This datum was taken at a modulation frequency of 1 kHz.

The modulation hysteresis discussed for the Version I device was also measured for device #4, and the result is shown in Figure 27. There is again an apparent break in frequency, but the roll off with frequency is greatly reduced from that measured without the SiO_2 buffer layer. The reason for this change in roll off is not understood.

The amplitude response on the modulation characteristic was measured for switch #4 and is plotted in Figure 28. The measured bandwidth is ∿250 mHz. At higher frequencies, there were a couple of resonances; this is characteristic of parasitic impedances. With proper packaging, the devices should have the designed gigahertz bandwidth.

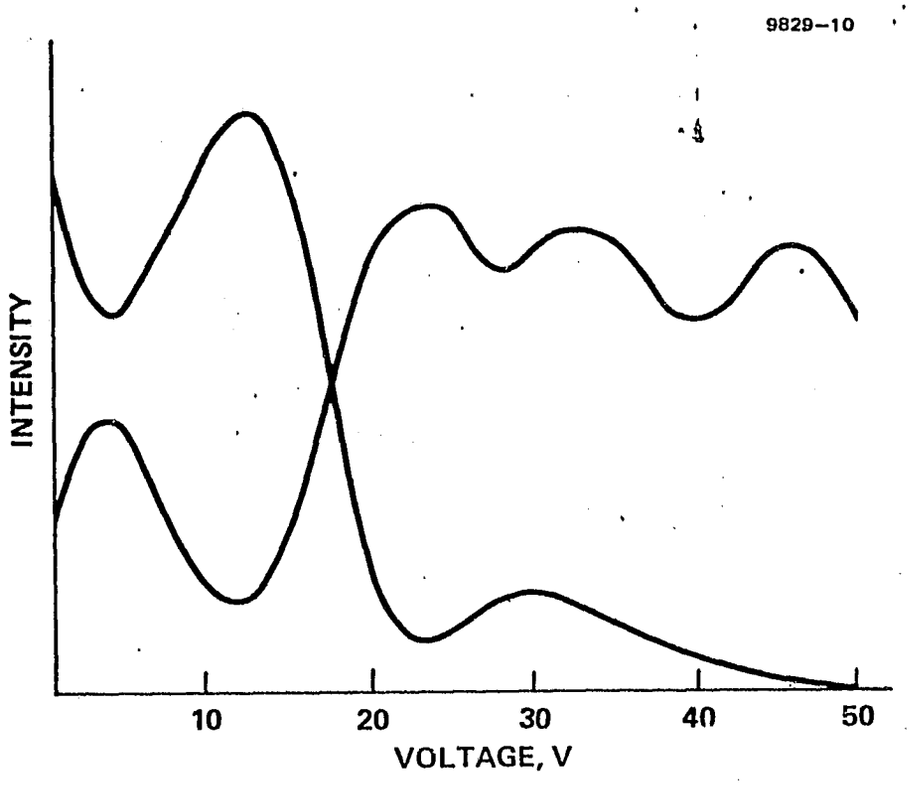

Figure 24(a). $\Delta\beta$ reversal switch characteristic for sample #4.

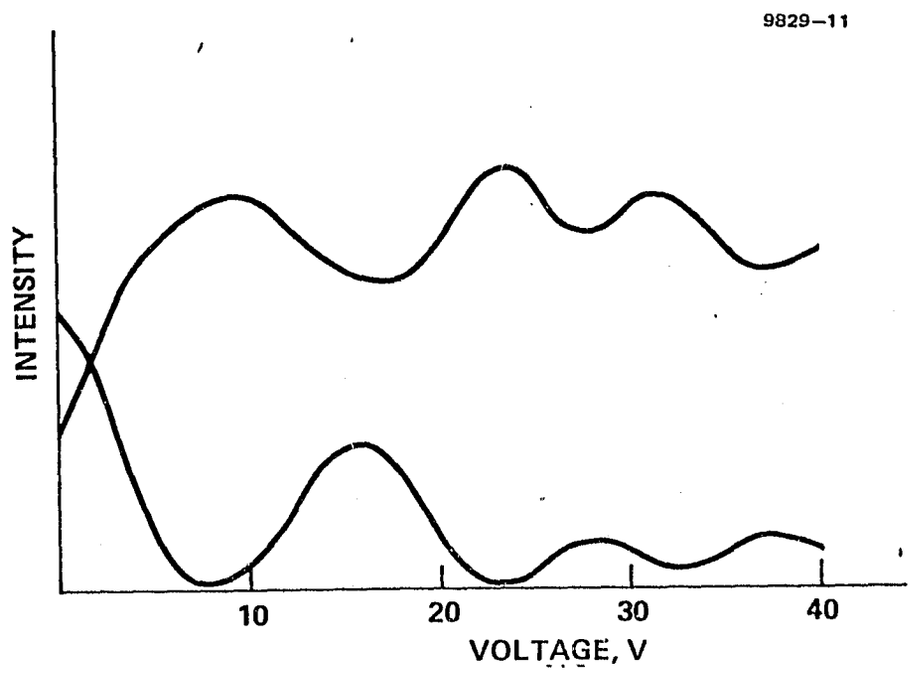

Figure 24(b). Conventional switch characteristic for sample #4.

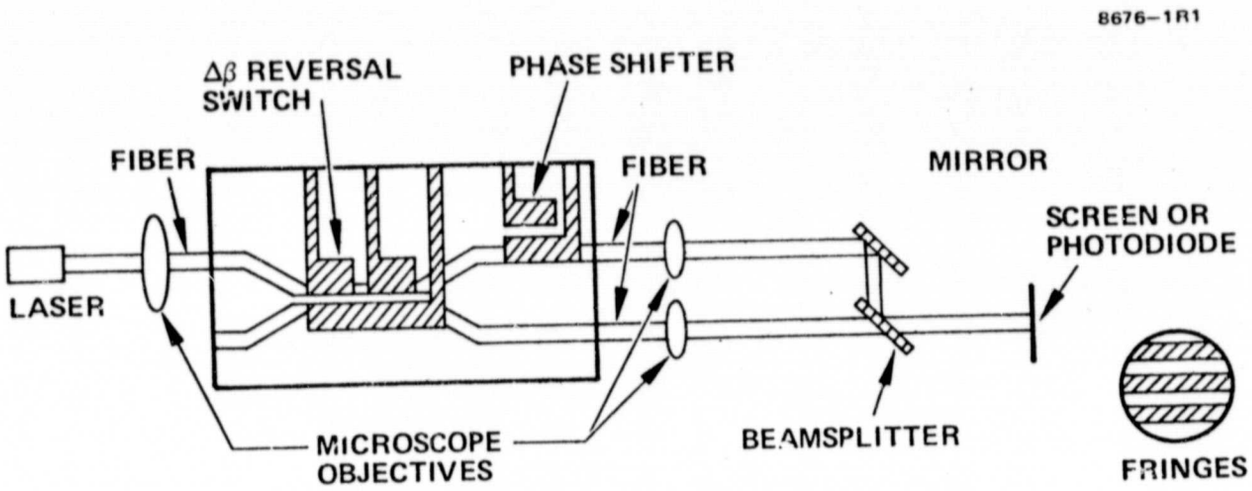

Figure 25. Phase shifter experimental test configuration.

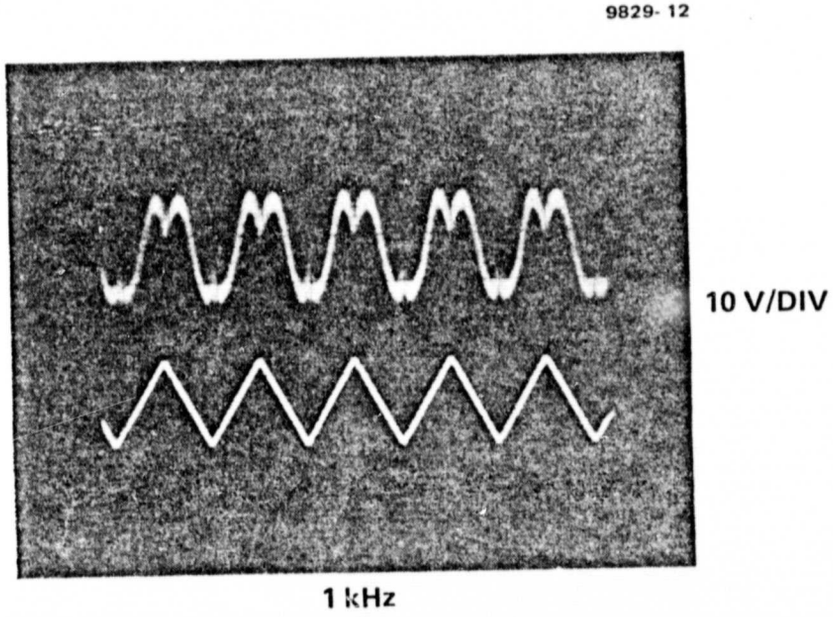

Figure 26. Oscillograph showing applied voltage (triangular wave) and measured fringe shift. The measurement was made at a 1 kHz modulation frequency.

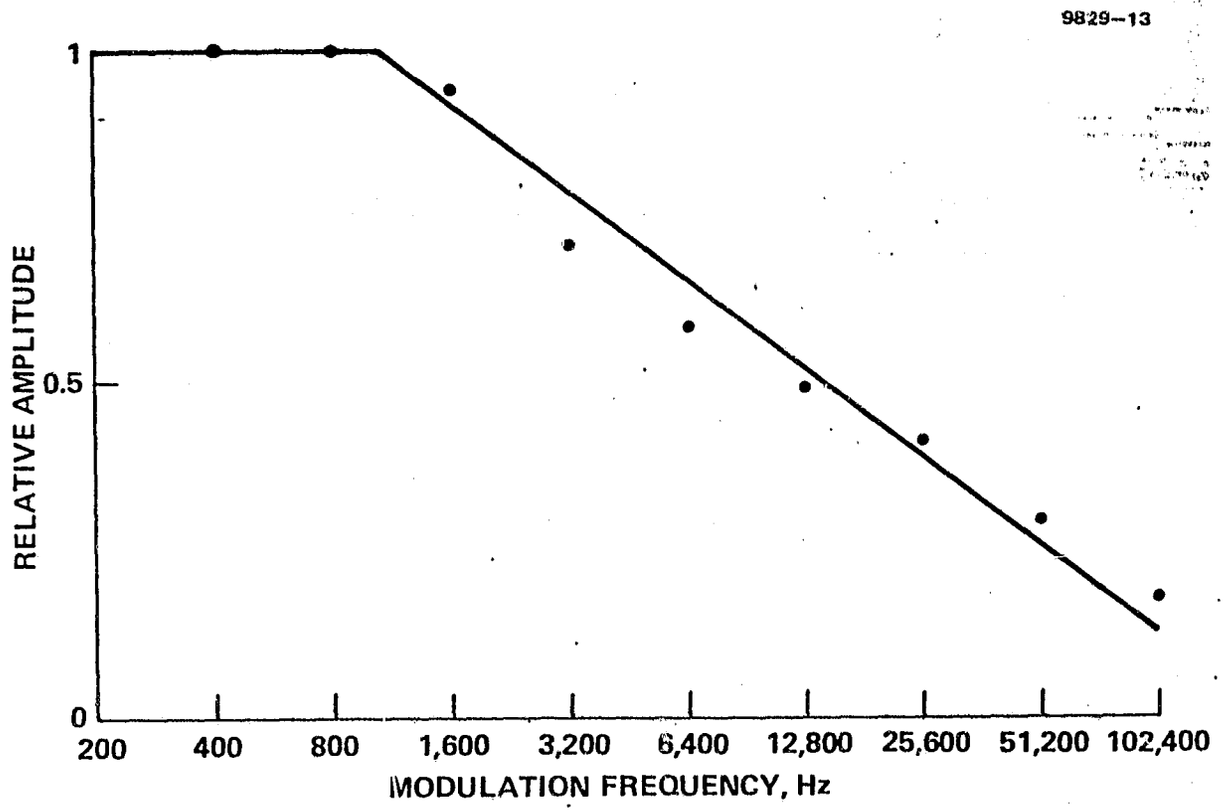

Figure 27. Modulation hysteresis amplitude versus frequency for sample #4.

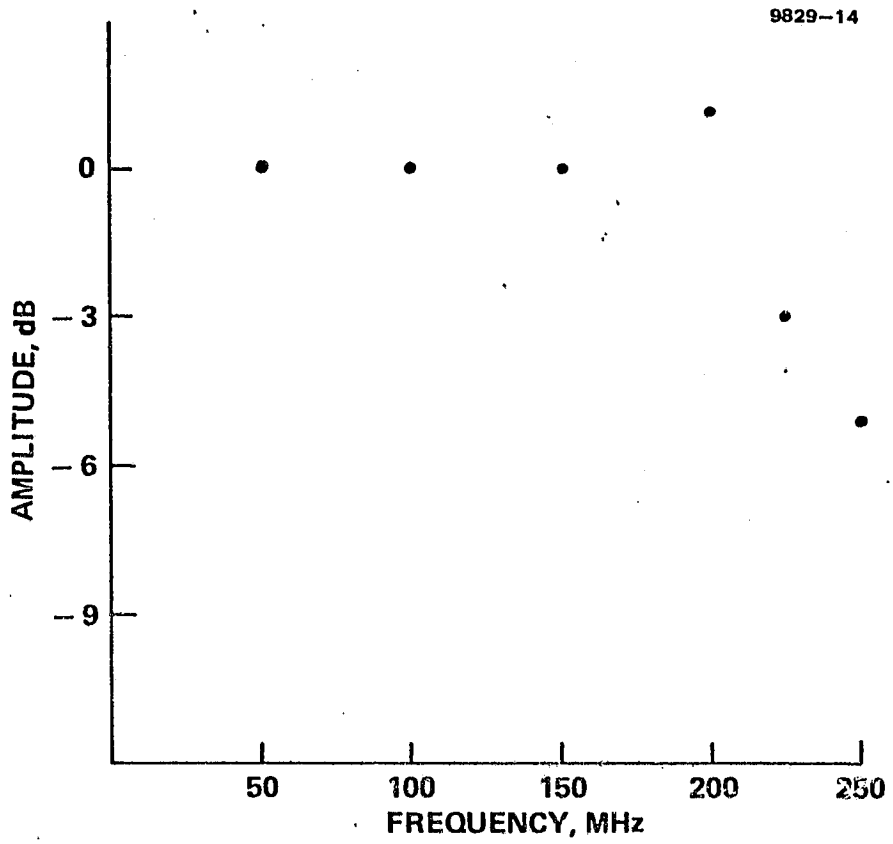

Figure 28. Modulation amplitude response versus frequency response for sample #4.

SECTION 4

POTENTIAL IMPROVEMENTS

A. INTRODUCTION

The present devices have two obvious drawbacks. First, the switching voltages are higher than desired. Second, the insertion loss from the fiber to chip is much higher than theoretically predicted. This section discusses these problems and the work that we believe is required to overcome them.

B. INSERTION LOSS REDUCTION

The insertion losses associated with hybrid devices are obviously dependent on several factors; these losses occur in the $LiNbO_3$ chip (waveguide losses) and at the interfaces between fiber and $LiNbO_3$. The chip losses, discussed above, are presently believed to be under control. Therefore, the major losses measured in the present devices are believed to occur at the interface between fiber and chip. The theoretically determined loss between fiber and waveguide is $\sim$1.5 dB. Currently, we measure losses that are typically much higher than this.

The excess loss problem has no simple solution other than a detailed study of the fabrication techniques involved (i.e., each step in the fabrication must be investigated thoroughly). In such a study, we would have to isolate the source of the losses and establish techniques for testing each component to eliminate the losses. The experiments we are presently conducting to reduce loss are discussed below.

Two tests have been proposed for establishing the source of the losses at the fiber/chip interface; they are to directly couple fiber to fiber and to directly couple chip to chip. If the edges are prepared properly, both of these configurations theoretically result in 100% throughput or no loss. Both of these experiments have been attempted, but the reproducibility of the results are less than satisfactory. This lack of reproducibility indicates that work is required to develop our polishing techniques and fiber holder fabrication.

After the polishing techniques have been improved, a test procedure must be established to test each component prior to introduction into a device. This procedure will require establishing a set of standard components with which the testing will be done.

During a series of experiments, an AR coating was placed between the fiber and $LiNbO_3$ chip to reduce or eliminate the reflections due to the index mismatch between the fiber ($\sim$1.48) and $LiNbO_3$ ($\sim$2.2). This reflection causes approximately a 4% loss per surface. The coating that we are presently investigating requires no air gap and is placed on the $LiNbO_3$ edge. The AR coating was designed using the average refractive index of $LiNbO_3$ at 0.85 μm and a fiber index of 1.48. Table 3 shows the resulting reflections for variations from these values. The coating is 0.0975/0.0556 λ thickness of ThF_5/ZnSe. This coating has been deposited and tested; the result was a 0.1% reflection.

C. SWITCHING VOLTAGES

Several techniques are available to produce waveguide switches with reduced switching voltages. These techniques include TM propagation in z-cut $LiNbO_3$; TE propagation in y-cut $LiNbO_3$; multistage $\Delta\beta$ reversal; a Mach Zender with a long interaction length; and any appropriate combination of these. However, each technique has technical difficulties that need to be investigated.

In the switches fabricated to date, we have primarily used z-cut $LiNbO_3$ samples and TE mode propagation. It would be preferable to use y-cut substrates with TE mode propagation along the x direction or z-cut substrates with TM mode propagation. Either of those two configurations would allow designs with the r_{33} electrooptic coefficient, which is 3.5 times larger than the r_{31} coefficient presently utilized.

The major problem in implementing the TM mode propagation in z-cut material is the loss due to the electrodes placed directly on the waveguides. This problem has been partially overcome recently by placing an SiO_2 layer between the $LiNbO_3$ and the electrodes (see the discussion of device 2 in Section 3). In y-cut material, the electrodes are not placed on the waveguides, but an electrode must be placed between the guides. This electrode would need to be small and hence would be difficult to make.

Table 3. AR Coating

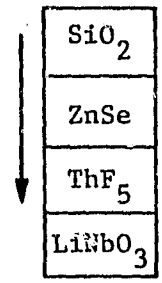

λ = 0.850 μm

SiO_2 n	$LiNbO_3$ n	2.18075	2.224	2.26 n
1.46	% Ref 1/Surf	0.016	0.002	0.006
1.47		0.011	0.000	0.008
1.48		0.010	0.001	0.011

Another problem with these configurations is the presence of the planar out-diffused modes; these modes compete with the excitation of the channel modes and contribute to crosstalk. We feel that this may not be as large a problem as has been thought. Even so, we are working on ways of compensating for the Li_2O depletion; this work is described below.

As pointed out in Section 2, a multiple (greater than 2) $\Delta\beta$ reversal section can be used to reduce the switching voltages. We are presently working on switches (using IR&D funds) at a wavelength of 0.85 μm with four sections. This electrode configuration should reduce our switching voltages to ~15 V for the TE mode in z-cut $LiNbO_3$ and 5 V for the TM mode.

Another method that has been proposed for making switches is a combination of the $\Delta\beta$ reversal and Mach Zender configurations. This

proposed switch configuration is shown schematically in Figure 29. A relation between the input (R_o, S_o) and output (R,S) light amplitudes is

$$\begin{pmatrix} R \\ S \end{pmatrix} = \begin{pmatrix} C & -jD \\ -jD^* & C^* \end{pmatrix} \begin{pmatrix} R_o \\ S_o \end{pmatrix} . \tag{24}$$

$$C = A_1 A_1^* A_2 - B_1 B_1^* A_2^* \tag{25}$$

$$D = 2\, A_1 B_1 \cos L_2 \delta_2 \tag{26}$$

$$A_1 = \cos\left(L\sqrt{k^2 + \delta^2}\right) + \frac{jG\sin\left(L\sqrt{k^2 + \delta^2}\right)}{\sqrt{k^2 + \delta^2}} \tag{27}$$

$$B_1 = \frac{k\sin L\sqrt{k^2 + \delta^2}}{\sqrt{k^2 + \delta^2}} \tag{28}$$

$$A_2 = \cos L_2\delta_2 + j\sin L_2\delta_2 \quad , \tag{29}$$

where k is the coupling coefficient in regions I and III, δ is one-half the difference between the propagation constants in guides 1 and 2 due to the applied voltages $(|\beta_1 - \beta_2|/2 = \delta)$ in regions I and III, L is the length of regions I and III, L_2 is the length of region 2, and δ_2 is one-half the difference between the propagation constants in guides 1 and 2 due to the applied voltages in region 2. The coupling coefficient in region II is assumed to be zero; this can be achieved either by ion milling a groove between the guides in Region II or by physically separating the guides. Regions I and III are the $\Delta\beta$ reversal sections; Region II is the Mach-Zender.

If $\delta_2 = 0$, then Eqs. 24-29 become those of the $\Delta\beta$ reversal switch having a cross state when $C^2 = 0$. The locus of curves for which this is

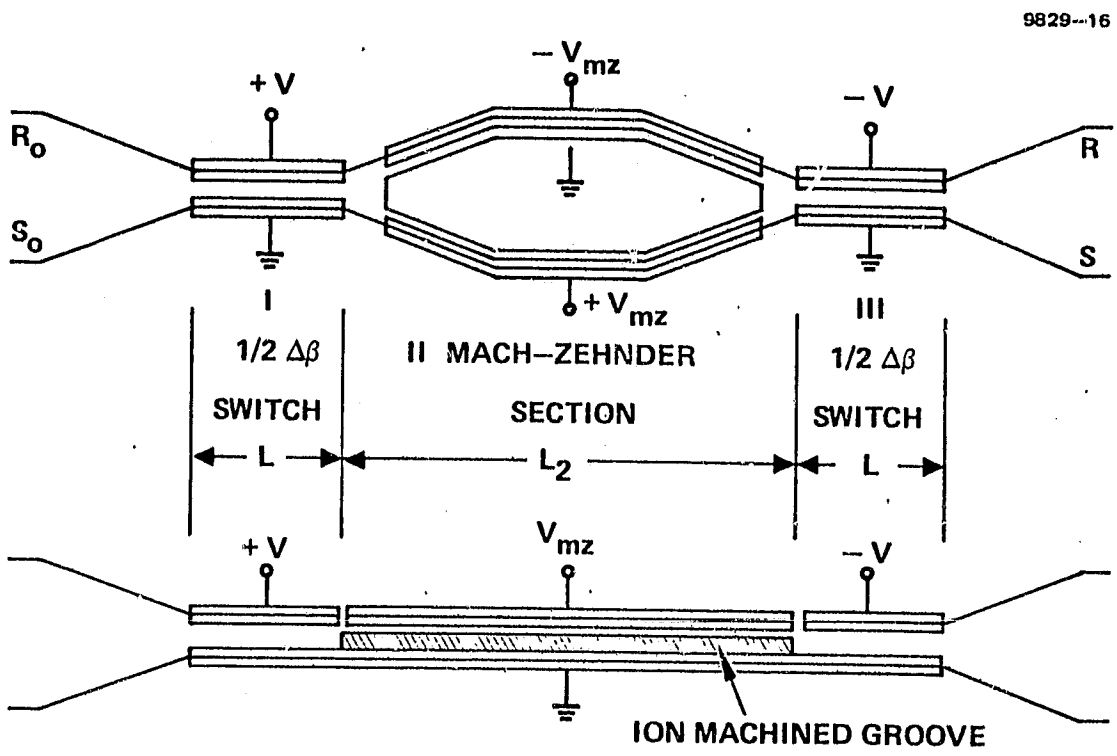

Figure 29. Two configurations for the Δβ reversal-Mach Zender combined switch.

true is shown in Figure 4. A parallel state is achieved by forcing D to zero. This can be achieved by applying a voltage to electrode II, forcing $L_2\delta_2 = \pi/2$, and keeping the voltages to electrodes I and III constant. The voltage required to accomplish this is significantly less than the voltage required to achieve the switching by changing the voltages in sections I and II. This configuration is being worked on with IR&D funds and is Hughes proprietary.

D. SUPPRESSION OF Li_2O OUT-DIFFUSION

A major problem in waveguide formation in $LiNbO_3$ by Ti metal in-diffusion is that, at high diffusion temperatures (850 to 1100°C), the crystalline substrate suffers the loss of loosely bound Li_2O through a surface out-diffusion process. The deviation from crystal stoichiometry at the wafer surface increases the extraordinary refraction index and leaves the ordinary refractive index unchanged. As a result, there is a planar waveguide formed due to Li_2O out-diffusion in addition to the waveguide formed by metal in-diffusion. This out-diffusion waveguide can confine a TE polarization wave for propagation along the X axis on a y-cut wafer (or Y axis on an x-cut wafer). In a z-cut wafer, TM polarization waves propagate in the out-diffused layers. In active channel waveguide devices, the channels are usually aligned to the X axis in y-cut material such that the largest electrooptic coefficient, r_{33}, can be used for TE polarization modes. However, the existence of the planar out-diffusion waveguide introduced excess crosstalk between channels. Furthermore, in an end-butt coupling configuration between a channel waveguide and a single-mode optical fiber or a diode laser source, a large portion of the optical energy is coupled to these unwanted out-diffusion modes, which are excited easily by the input light source.

We are developing a technique for eliminating Li_2O out-diffusion waveguides by annealing the crystal in $LiNbO_3$ powder.[10] The mechanism of the Li_2O compensation process is explained as follows. At high temperature, the loosely bound Li_2O molecules tend to escape from the surface. Since $LiNbO_3$ powder has more surface area than $LiNbO_3$ wafers, the Li_2O vapor pressure due to the powder is sufficient to build up an

Li_2O-rich environment so that the out-diffusion process from the $LiNbO_3$ wafer is suppressed. Furthermore, the compensation process in which Li_2O is in-diffused into a lithium-deficient $LiNbO_3$ wafer becomes thermodynamically favorable (Figure 30).

We have successfully eliminated the Li_2O out-diffusion mode in a y-cut sample of $LiNbO_3$. The experiment we conducted is as follows. First, a sample had 5-, 7-, 9-, 11-, and 13-μm-wide guides formed with 500 Å of Ti evaporated on the surface. The sample was cut into two samples and had the edges polished and guides tested. Both samples were rediffused at 1000°C for 6 hours. The first was rediffused in an oxygen atmosphere, the second in an Li_2O-enriched atmosphere by placing the sample in a Pt box containing $LiNbO_3$ powder. On testing, the second sample had no out-diffusion guide. The following additional information was obtained from the samples:

Before Second Diffusion (both samples)

Guide Width	$TE_{1,2}$	$TM_{1,2}$
5 μm	single mode	cutoff
7 μm	single mode	cutoff
9 μm	multimode	single mode
11 μm	multimode	single mode
13 μm	multimode	single mode

After Second Diffusion

Guide Width	TE_1	TE_2	TM_1	TM_2
5 μm	single mode	cutoff	cutoff	cutoff
7 μm	multimode	cutoff	cutoff	cutoff
9 μm	multimode	single mode	single mode	single mode
11 μm	multimode	single mode	single mode	single mode
13 μm	multimode	single mode	single mode	single mode

These data indicate some very interesting trends in the guide index induced by the out-diffusion treatment:

- The TM modes have little variation in mode structure (i.e., the ordinary index is only slightly if at all affected by the treatment).
- The TE modes have been changed dramatically. These changes indicate that the extraordinary Δn induced by the Ti reduced dramatically on elimination of the out-diffusion mode.

Another effect noticed that is significant is the difference between this sample and the z-cut sample with the same guides. The TE modes for this sample were single mode for the 5- and 7-μm widths and multimode for the other widths. These modes correspond to Δn_o (i.e., the change in the ordinary refractive index). The corresponding guides in the y-cut sample are cutoff for the 5- and 7-μm widths and single mode for the other widths.

Although we have successfully demonstrated that the process will work, there is still a considerable amount of effort required before this fact can be applied to a device. This is primarily due to the fact that previous experience cannot be applied directly.

SECTION 5

CONCLUSIONS AND RECOMMENDATIONS

During this program, we have designed, fabricated, tested, and delivered four integrated-optic waveguide circuits with a phase bias element and modulator on the same chip. The chips were addressed by single-mode fibers, with fiber pigtails affixed to the chips. The intended application of these chips is for use in the fiber-optic gyro presently under development at JPL.

The technology development was divided into two phases: chip development (involving the development of the 10 chip with the 2 x 2 switch and phase shifter combination) and fiber-to-chip interfacing (involving the permanent coupling of single-mode fiber-optic pigtails to the four ports of the chip. The theory and design involved in these phases is described in detail in Section 2. The switch and chip performance is described in Section 3. Finally, potential improvements are discussed in Section 4.

The switch format was based on coherent coupling of the light between waveguides formed in Z-cut $LiNbO_3$. The control of the coupling was achieved by electrooptically varying the phase propagation constants of each guide. The electrode arrangement divides the coupler into two equal-length sections, such that the ΔB reversal[2] technique could be used to achieve both the bar and cross state. Using this technique, we have demonstrated switching voltages between 50 and 60 V for the 0.85 μm wavelength for the TE propagating mode. For the TM propagating mode, switching voltages of less than 25 V have been demonstrated. To reduce the switching voltages further, one of several approaches can be taken; these approaches are discussed in Section 4. In all cases, the basic variable is the length of the interaction length.

The goal of the phase shifter (a phase shift of $\pi/2$ in response to 15 V or less for 0.85 μm operation) was achieved by electrooptically varying the phase propagation constant of one guide independent of the other.

Task 3: Low-Voltage Switch

Research should be conducted to develop a low-voltage switch using guides that are optimized for laser- and fiber-to-chip coupling. The low-voltage switch would most probably be a multisection $\Delta\beta$ reversal switch.

Task 4: Chip Definition, Fabrication Test, and Delivery

Having conducted Tasks 1, 2, and 3, the required technical knowledge and expertise will be available to successfully design and fabricate a chip that will be useful to the fiber-optic rotation sensor. It is believed that this initial chip should be the minimum necessary to advance the state of the art of the gyro.

REFERENCES

1. W. Goss and R. Goldstein, Opt. Eng. 18, 9 (1979).

2. H. Kogelnik and R.V. Schmidt, IEEE J. Quantum Electronics QE-12, 1396 (1976).

3. J.F. Nye, Physical Properties of Crystals (Oxford at the Clarendon Press, London, 1957).

4. R.J. Pressley (Ed), Handbook of Lasers (Chemical Rubber Company, Cleveland, 1971).

5. E. Marcatili, Bell System Tech. J. 48, pp 2071-2102, Sept. 1969.

6. R.V. Schmidt, and R.C. Alferness, IEEE Transactions on Circuits and Systems, CAS-26, 12, December 1979, p. 1099.

7. I.P Kaminow, L.W. Stulz, and E.H. Turner, Appl. Phys. Lett. 27, 555 (1976).

8. W.K. Burns and G.B. Hocker, Appl. Opt. 16, 2048 (1977).

9. L.G. Cohen, Bell Syst. Tech. J., March 1972, p. 573.

10. B. Chen and A.C. Pastor, Appl. Phys. Lett. 30, 570 (1977).